Ultra-strong metallic glasses by knowledge based alloying guidelines

Von der Fakultät für Georessourcen und Materialtechnik der

Rheinisch-Westfälischen Technischen Hochschule Aachen

zur Erlangung des akademischen Grades eines

Doktors der Naturwissenschaften

genehmigte Dissertation

vorgelegt von **Dipl. Phys.**

Mathias von Avenarius (geb. Köhler)

aus Siegen

Berichter: Prof. Dr.-Ing. Dierk Raabe

Univ.-Prof. Jochen M. Schneider, Ph.D.

Tag der mündlichen Prüfung: 20. Dezember 2016

Abstract

As their name already implies, metallic glasses (MGs) exhibit metallic properties like electrical and thermal conductivity, moderate ductility and a lustrous surface, while featuring amorphous characteristics, such as the absence of periodic long range order. The possible property combinations of these two materials science fields cause metallic glasses to be of great interest for current research. The objective of this thesis is to link mechanical properties of metallic glasses, such as stiffness, strength and toughness, to the underlying chemical bond structure and overall topology of the investigated specimen.

Based on theoretical considerations derived from molecular dynamics (MD) simulations, melt spinning or magnetron sputtering is used to synthesize a variety of Co-based and non-Co-based metallic glasses. The amorphous state of the as prepared metallic glasses is proved by atom probe tomography (APT), transmission electron microscopy (TEM), X-ray diffraction patterns (XRD) and differential scanning calorimetry (DSC). The structural analysis is done by APT and high-energy X-ray experiments. Young's modulus, hardness, fracture toughness and fracture strength of the synthesized metallic glasses are investigated by nanoindentation and micro cantilever bending tests. Very high stiffness of E_{red} =344 GPa and fracture strength σ =11 GPa are reported for a combinatorial $Co_{39.2}Ta_{5.8}B_{55.0}$ metallic glass composition, exceeding the so far reported world record metallic glasses [1, 2].

The MD simulations model developed by Hostert et al. [3] for predicting elastic properties of metallic glasses is tested and validated for the compositions and synthesis methods utilized within this thesis. Lewandowski et al. [4] proposed a sharp transition from ductile to brittle at a Poisson's ratio of ν =0.32, which is not observed for the metallic glasses investigated in the course of this work. Therefore, the Poisson's ratio is not a sufficient criterion to predict the toughness of metallic glasses and, instead, a new model, based on the bonding nature and the electronic structure of the alloying elements, is proposed: The proportion of bonds, originated from deep core, hybridized states compared to the overall bonding, is a much more reliable indicator for the damage tolerance of metallic glasses.

The responsible deformation mechanism in metallic glasses is governed by shear bands and their formation and evolution is not fully understood, yet. Hence, shear bands of a heavily deformed amorphous $Al_{88}Y_7Fe_5$ system are investigated by correlative TEM/APT experiments. The compositional changes of shear bands are determined by APT, while the relative density changes are recorded by TEM [5]. It is concluded that material transport is happening within different parts of a shear band, which results in density variations along its propagation direction, while the matrix is unaffected.

Zusammenfassung

Wie ihr Name bereits impliziert, weisen metallische Gläser (MGs) sowohl metallische Eigenschaften, wie elektrische und thermische Leitfähigkeit, moderate Duktilität und eine glänzende Oberfläche auf, besitzen aber auch amorphen Charakter, wie die Abwesenheit von langreichweitiger periodischer Ordnung. Die Möglichkeit Eigenschaften aus diesen zwei Wissenschaftsbereichen zu kombinieren begründet das große Interesse der aktuellen Forschung an diesen Materialien. Das Ziel dieser Dissertation ist, die mechanischen Eigenschaften, wie Steifigkeit, Festigkeit und Zähigkeit mit den zugrundeliegenden chemischen Bindungsstrukturen und der Probengeometrie zu verknüpfen.

Basierend auf theoretischen Überlegungen welche von MD Simulationen abgeleitet sind, werden eine Vielzahl von Co-basierten und nicht Co-basierten metallischen Gläsern durch Schmelzschleudern und Magnetron Sputtern synthetisiert. Der amorphe Grundzustand der hergestellten metallischen Gläser wird durch Atomsondentomographie (APT), Transmissionselektronenmikroskopie (TEM), Rötgenbeugung (XRD) und dynamische Differrenzkalorimetrie (DSC) sichergestellt. Die Strukturanalyse wird mittels APT und hoch energetischer Röntgenbeugung durchgeführt. Das Elastizitätsmodul, die Härte, die Bruchzähigkeit und die Bruchfestigkeit der synthetisierten metallischen Gläser wird mittels Nanoindentation und mikro Biegebalken Tests bestimmt. Eine sehr hohe Steifigkeit von E_{red} =344 GPa und eine Bruchzähigkeit von σ =11 GPa werden für ein kombinatorisches $Co_{39.2}Ta_{5.8}B_{55.0}$ metallisches Glas berichtet, was die bisherigen Weltrekordgläser übertrifft [1, 2].

Das MD Simulationsmodell von Hostert et al. [3] zur Vorhersage von elastischen Eigenschaften metallischer Gläser wird für die verwendeten Kompositionen und Herstellungsmethoden innerhalb dieser Arbeit getestet und bestätigt. Lewandowski et al. [4] schlugen einen sprunghaften Übergang von duktil zu spröde bei einer Poissonzahl von ν =0.32 vor. Dies wird an den metallischen Gläsern der vorliegenden Arbeit nicht beobachtet. Daher ist die Poissonzahl kein hinreichendes Kriterium für die Vorhersage von Zähigkeit bei metallischen Gläsern. Stattdessen wird ein neues Modell, basierend auf den Bindungstypen und der elektronischen Struktur der Legierungselemente, vorgeschlagen. Die Anzahl der kernnahen, hybridisierten Bindungszuständen im Verhältnis zu den Gesamtbindungszuständen ist ein verlässlicherer Indikator für die Schadenstoleranz von metallischen Gläsern.

Der wesentliche Verformungsmechanismus in metallischen Gläsern wird durch Scherbänder und deren Entstehung und Verlauf geprägt und ist bisher nicht vollständig verstanden.

Daher werden Scherbänder eines stark verformten amorphen $Al_{88}Y_7Fe_5$ Systems mittels korrelativen TEM/APT Experimenten untersucht. Die kompositionellen Veränderungen der Scherbänder werden mittels APT bestimmt, während die relativen Dichteänderungen mittels TEM aufgenommen werden [5]. Es wird geschlussfolgert, dass Materialtransport innerhalb der verschiedenen Teile eines Scherbandes stattfindet, was in Dichteänderungen entlang der Scherband Ausbreitungsrichtung resultiert, während die Matrix nicht betroffen ist.

Preface

This thesis contains work done within a collaboration of the Max-Planck-Institut für Eisenforschung GmbH (MPIE) in Düsseldorf and the Materials Chemistry department of the RWTH Aachen University. The financial support of the Deutsche Forschungsgemeinschaft (DFG) as part of the SPP-1594 "Quantum mechanically guided design of ultra-strong glasses" is gratefully acknowledged.

Parts of the sample fabrication (melt spinning) and the structural and chemical characterisation by transmission electron microscopy (TEM), X-ray diffraction (XRD) and atom probe tomography (APT) as well as the mechanical properties investigations were carried out by the author at the MPIE.

The MD simulations and thin film synthesis by sputtering were provided by the Materials Chemistry department of the RWTH Aachen University who in collaboration with the Deutsche Elektronen Synchrotron (DESY) conducted the structural synchrotron experiments.

The following papers are the foundation of this work:

I. Köhler, M., Schnabel, V., Kontis, P., Chen, Y.-T., Soler, R., Kirchlechner, C., Dehm, G., Raabe, D. & Schneider, J. M.
„Outstanding mechanical properties in combinatorial Co-based metallic glass thin films caused by geometrical constraints." *manuscript in preparation*

II. Köhler, M., Kontis, P., Kirchlechner, C., Herbig, M., Liebscher, C., Dehm, G. & Raabe, D.
„Investigation of shear bands in $Al_{88}Y_7Fe_5$ by correlative atom probe tomography and transmission electron microscopy." *manuscript in preparation*

III. Schnabel, V., Jaya, B. N., Köhler, M., Music, D., Kirchlechner, C., Dehm, G., Raabe, D. & Schneider, J. M.
"Electronic hybridisation implications for the damage-tolerance of thin film metallic glasses." *Scientific Reports (2016)*

Acknowledgement

For a successful PhD thesis and the related experimental and theoretical work the help and support of many people is required. Colleagues, supervisors, technicians, friends and family contribute a lot of time, patience and knowledge for such an accomplishment and I want to thank all of them. A couple of important people who accompanied me during my PhD time deserve to be mentioned in particular:

- First of all, I want to thank Prof. Dierk Raabe for his continuous support and advice. Certainly, I also thank him for the opportunity of doing my PhD at the Max-Planck Institut für Eisenforschung. It always astonished me how it is possible for him to keep track of each individual PhD student he is supervising.

- Many thanks also go to my co-advisor Prof. Jochen M. Schneider, who helped pushing the project with valuable discussions and new ideas. The close collaboration and various meetings at the materials chemistry department in Aachen were very inspiring and productive. Therefore, thanks also go to Volker Schnabel.

- Also I want to thank my two direct supervisors Pyuck Choi and Baptiste Gault, who gave me a deeper introduction into the magical world of atom probe tomography and helped whenever APT reconstructions caused trouble.

- Furthermore, I want to thank all current and former colleagues and technicians at the Max-Planck Institut für Eisenforschung: Jaya Balila, Daniel Haley, Jake Benzing, Michael Herbig, Andreas Stoffers, Rafael, Andreas Sturm, Uwe Tezins, Monika, Heidi, Katja, Lars, Rita, Meimei, Mengji, Zahra, Stefan Hieke, Wei Guo, Paul, Torsten, Emanuel, Ivan, Christoph Kirchlechner, Paris and all the people I forgot. Especially, I want to thank my office mates Lutz, Christian and Anja.

- Special thanks, of course, go to my parents and siblings for their continuous support and patience.

- Last but not least, I want to thank my little family, containing of my wife Andrea and son Jakob. Due to my wife’s big support and the mostly quiet nights little Jakob allowed us, it was possible to finish this thesis without falling asleep at work.

Finally, the financial support of the Deutsche Forschungsgemeinschaft (DFG), as part of the SPP-1594, is gratefully acknowledged.

Contents

Contents

List of abbreviations and symbols

APT	atom probe tomography
BF	bright field
BMG	bulk metallic glass
CTA	contingency table analysis
DC	direct current
DF	dark field
DFT	density functional theory
DSC	differential scanning calorimetry
EDX	energy dispersive X-ray spectroscopy
FIB	focused ion beam
HAADF	high-angle annular dark field
LEFM	linear elastic fracture mechanics
MD	molecular dynamics
MG	metallic glass
NBDP	nanobeam diffraction patterns
NI	nanoindentation
OpenMX	open source package for Materials Explorer
PDF	pair distribution function
RDF	radial distribution function
RF	radio frequency
SEM	scanning electron microscopy
SRO	short range order
STEM	scanning transmission electron microscopy
STZs	shear transformation zones
TEM	transmission electron microscopy
TTT	time-temperature-transformation
UHV	ultra-high vacuum
VASP	Vienna ab initio simulation package
XFEM	extended finite element method
XRD	X-ray diffractometry

List of abbreviations and symbols

a_c	critical defect size
B	bulk modulus
E	Young's modulus
E_{red}	reduced Young's modulus
F	electric field
G	shear modulus
G_f	fracture energy
h	Planck's constant
h_c	contact depth
k_f	field factor
$K_{I,C}$	fracture toughness
M	molar mass
m/n	mass to charge ratio
R	tip radius
r^*_p	plastic zone size
T_g	glass transition temperature
$\Delta\rho$	relative density
λ	wavelength
μ	Pearson's coefficient
ν	Poisson's ratio
σ	fracture strength
ξ	image compression factor
Z	atomic number

1. Motivation

Metallic glasses are a relatively new group of materials, showing a lot of potential in terms of mechanical and magnetic properties [6, 7]. They are investigated by the scientific community since their discovery in the early 1960's [8]. Recently, first commercial metallic glasses, such as the Vitreloy series [9], are available. Nevertheless, a lot of open questions regarding the fundamental deformation and formation mechanisms in these amorphous alloys remain.

In 2011 the Deutsche Forschungsgemeinschaft (DFG) started a priority program (SPP-1594) on metallic glasses, which enabled the financial support for this thesis and others. Today's continuous advances in computational power [10, 11] allows the scientific community to investigate or explain fundamental mechanisms in materials science by simulations and calculations [12]. The increasing computer power also gave a big boost or facilitates more complex experimental techniques, such as atom probe tomography (APT) reconstructions, computer controlled sample preparation methods (e.g. focused ion beam (FIB)), or enhances the possibility of image processing of all kinds of microscopes (e.g. transmission electron microscopy (TEM), scanning electron microscopy (SEM) and many others). This opens completely new and advanced possibilities for the investigations of metallic glasses among other materials. Therefore, it was a great and promising opportunity to use the state-of-the-art experimental equipment established at the MPIE and the computational expertise of our collaboration partners at the materials chemistry department of the RWTH Aachen University.

So far, existing alloying guidelines, like the proposed use of Poisson's ratio [13] as criterion for ductility or brittleness of metallic glasses, are not satisfying and many exceptions are reported in literature, as summarized by Schnabel et al. [14]. This thesis is part of a collaboration, whose objective is to develop universal knowledge based alloying guidelines for ultra-strong metallic glasses, using a combination of theoretical and experimental methods. The materials chemistry department of the RWTH Aachen University supported this work with MD simulations of mainly Co-based metallic glasses in order to predict their elastic properties and to derive bond characteristics. They also provided the investigated thin film metallic glasses, which were prepared by magnetron sputtering. Young's modulus, hardness, fracture toughness and fracture strength of synthesized metallic glasses are investigated by nanoindentation and micro cantilever bending tests, in order to evaluate the MD simulation results (elastic part). The amorphous state of the metallic glasses as prepared by thin film magnetron sputtering and melt spinning is proved by APT, TEM, X-ray diffraction patterns (XRD) and differential scanning calorimetry (DSC). In combination with high-energy X-ray experiments, performed by our collaboration partners, a general alloying guideline for the damage tolerance in metallic glasses is found: The proportion of bonds, which originate from deep core, hybridized states compared to the overall bonding can be used as guidance.

A second aspect of this work attends to the not yet fully understood deformation mechanism in metallic glasses, the shear banding. A good understanding of this mechanism might be essential to further improve mechanical properties of metallic glasses. Therefore, heavily deformed $A_{88}Y_7Fe_5$ metallic glass is investigated for the first time by correlative APT/TEM and individual shear bands are analysed. APT experiments reveal differences in chemical composition among shear band and matrix, while density variations are observed by TEM [5].

By helping to understand the fundamental mechanisms in metallic glasses, a declared goal is to make metallic glasses and their properties more beneficial and present in our daily life. So far, metallic glasses are only established for some special applications like micro gears [15], for inductor cores [16] or for medical applications (e.g. implants) [17, 18]. This is, basically, due to the limited dimensions of metallic glasses, which originates from the necessary fast quenching rates, making the synthesis and upscaling more complex. An increasing commercialization will lower the costs and support the research effort on metallic glasses.

The perspective to work on this interesting and young class of materials, combining state-of-the-art experimental and computational methods while having the opportunity for various collaborations within the SPP-1594 were the decisive reasons for picking this topic.

2. Introduction

Since 5000 BC metals are of great importance for mankind [19] as tools, weapons and structural materials and an end of their importance and development is not in sight. Especially in our present world, scientist and engineers are always looking for new materials with improved or specialized properties, better processability, lower costs or for completely new fields [20, 21] in order to comply the demands of industry and to drive progress. Although, other material classes like polymers, graphene or semiconductors seem to be more in the spotlight of scientific research and society, the consequent research and development of metals provides the foundation of the modern world we are living in today.

Until the middle of the last century metals and metallic alloys were only known and utilized in their crystalline form, because metals nucleate and grow crystalline phases fast and easily during the cooling process. In 1952 Turnbull et al. [22] predicted the existence of glassy phases for fast quenched metals.

2.1 Metallic glass

Metallic glasses are metals which have been cooled down from the liquid phase into a solid state while the structure of the molten phase is retained [23]. Therefore, metallic glasses are also called amorphous (Greek for no shape / no order) metals, which indicate its lack of inner periodic structure. Compared to crystalline materials metallic glasses show no highly ordered periodic atomic structure, like the long range order in a lattice. Nevertheless, they are not completely random and show a certain short-range-order (SRO) (<5 Å) and even medium-range-order (<300 Å), due to the principle of efficient filling of space in a solid [24, 25].

High cooling rates are necessary to prevent crystallisation within the sample. A material's ability to resist crystallisation is called glass forming ability and is defined by $\Delta T = T_x - T_g$ where T_x is the temperature at which the materials begins to crystalize and T_g is the glass transition temperature [26] and depends on the cooling rate [7]. A time-temperature-transformation (TTT) curve as described by Löffler et al. [27] visualizes this. From the TTT curve it is also obvious that heat treatment for enhancing the mechanical properties of metallic glasses is only possible in a narrow regime because structural changes like crystallisation can occur. The TTT curve in Figure 2-1 is a typical representative for the shape of theses curves in metallic glasses [28].

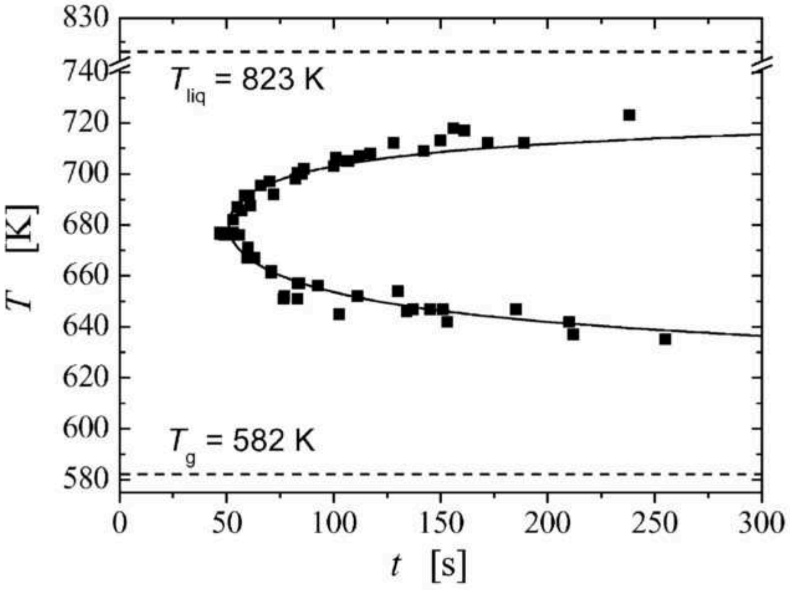

Figure 2-1: *Time-Temperature-Transformation (TTT) diagram of $Pd_{40}Cu_{30}Ni_{10}P_{20}$ by Löffler et al. [27].*

The procedure of quenching a molten metallic alloy rapidly into a “glassy” state solid was first performed by Klement et al. in 1960 [8]. They produced small flakes of $Au_{75}Si_{25}$ by splat quenching and proved the amorphous state by X-ray diffractometry XRD.

The necessary high cooling rates limit the dimensions of metallic glasses due to the thermal conductivity within the alloy. The transport of heat towards the surface must be sufficiently high so that the cooling curve does not pass the crystalline nose at any part within the sample. So far, the biggest produced samples are cylinders of $Pd_{40}Cu_{30}Ni_{10}P_{20}$ with a diameter of 72mm [29].

These limitations in size and processing of metallic glasses are the main barriers for establishing metallic glasses in our daily live, although, they show very interesting mechanical and soft magnetic properties [2, 30]. Also, they show good corrosion resistance due to the lack of grain boundaries or dislocations as fast diffusion pathways [26, 31].

2.1.1 Empirical glass mixing rules

Metallic glasses are a rather young group of materials and therefore no universal theory exists to predict, for example, their glass forming ability in alloys or their mechanical properties. Several empirical rules have been postulated which increase the glass forming ability of metallic glasses [25, 32]:

- Big atomic size difference (mismatch ≈12%) [33]
- Negative enthalpy of mixing [34]
- Multicomponent systems (deep eutectics) [23]

These rules and their influence on the glass forming ability of metallic glasses have widely been discovered by trial & error approaches, which requires a tremendous amount of resources.

During the last decades computers have become more and more powerful [35] which enables the scientific community to perform more sophisticated atomistic simulations and, therefore, a more knowledge-based design of materials, including metallic glasses.

2.1.2 Quantum mechanically guided design

The advantage and concept of the quantum mechanically guided design of metallic glasses is to understand the underlying mechanisms and tend towards a knowledge-based design of metallic glasses with improved properties.

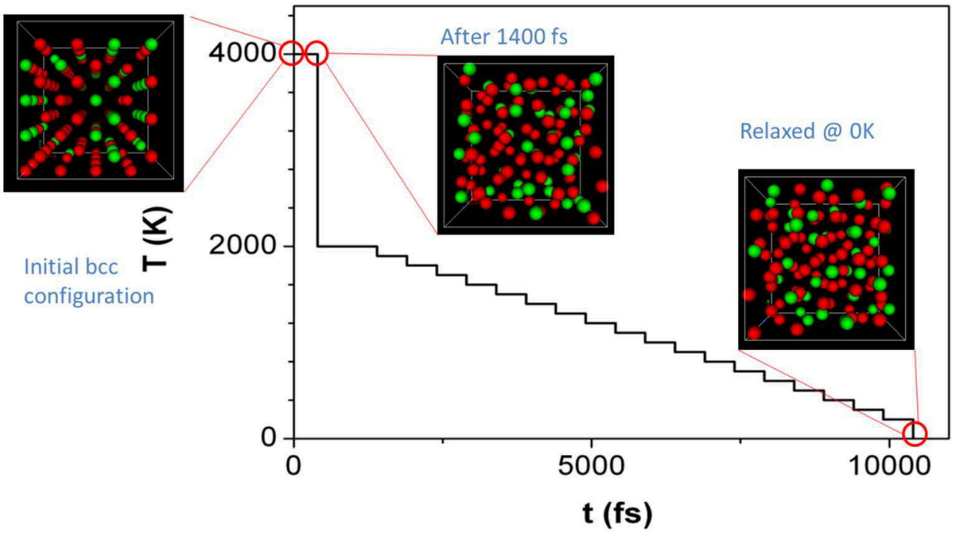

Figure 2-2: Principle of MD simulation process showing mixing of the atoms and the subsequent quenching process [3].

Previous work by C. Hostert et al. at the Materials Chemistry department of Prof. Schneider at RWTH Aachen University established and validated a model to study the correlation between the elastic properties of Co based metallic glass thin films and their electronic structure [3, 36]. *Ab initio* molecular dynamics based on density functional theory was used by applying the OpenMX code [37]. The initial configuration was set randomly on a bcc supercell and held at a temperature of 4000 K. After quenching the configuration was relaxed in terms of atomic positions and volumes. The elastic properties and density of states were determined by using the Vienna ab initio simulation package (VASP) code [38] on the relaxed and stress free configuration. The original work [3, 36] as well as the work by Schnabel et al. [39] (see Figure 2-3) shows good agreement in terms of density, elastic modulus and pair distribution function between *ab initio* molecular dynamic simulations and experimental data of sputtered Co based metallic glasses thin film.

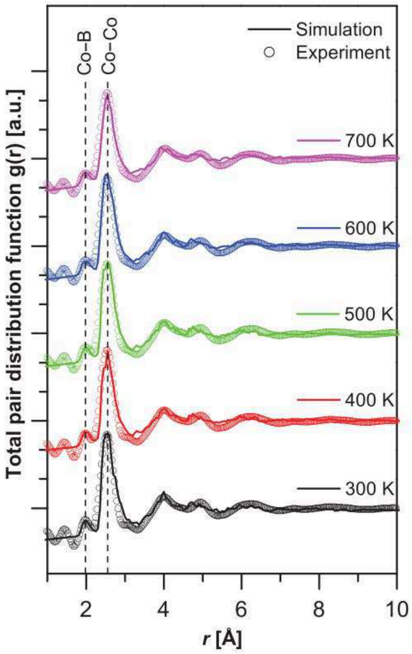

Figure 2-3 Total pair distribution functions of $Co_{67}B_{33}$ *metallic glass at different temperatures showing the good agreement between measured and simulated data [40].*

2.1.3 Deformation mechanism of metallic glasses

Because of the lack of any periodic order in metallic glasses their underlying deformation mechanism is different compared to polycrystalline materials. It was suggested by Argon et al. that atoms of amorphous materials below T_g and under shear can locally rearrange within the limits of the "free volume" into so called shear transformation zones (STZs) [41]. These STZs are the nuclei for the resulting macroscopic shear bands.

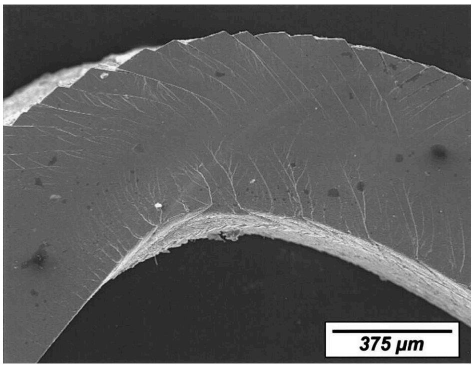

Figure 2-4: SEM melt spun ribbon Vitreloy 106 showing shear bands [42].

The "free volume" can be described as density fluctuations within the atomic structure of the metallic glass [43]. The atoms within a STZ are able to rearrange because the bonding type of metallic glasses is primarily of metallic character. Therefore, atomic bonds can be broken without the limitations of covalent bonds, which have to stick to certain bond angles, or ionic bonds, where the balance of charges applies [44].

STZs are point defect like defects [45] and their dimensions are in the range of $<6\ \text{nm}^3$ [46], while shear bands show dimensions of 10 – 20 nm in thickness and several 100 nm in length [47]. Shimizu et al. used computer simulations to demonstrate the formation of shear bands from STZs [48]. Due to external loading of the metallic glass, a group of STZs is activated at local inhomogeneity's, such as defects, cavities or impurities. An embryonic shear band nucleates from the group of STZs and as soon as the embryonic shear band reaches a critical length of ≈100 nm, it propagates and forms into a mature shear band. These shear bands form in an angle of ≈45° to the applied stress axes [49] as seen in Figure 2-4. They are the observable fundamental deformation mechanisms in metallic glasses for temperatures below T_g and high stresses (see Figure 2-5).

Processing conditions (e.g. method, cooling rate) have a tremendous influence on the mechanical properties [50]. This is due to the different amounts of "free volume" within the different metallic glass samples which results into varying generation of STZ as a response on external mechanical deformation.

Figure 2-5 shows, that at high temperatures (compared to T_g) and low stress, homogenous plastic flow occurs which is interesting for shaping and processing metallic glasses. This "region" is not of further relevance for this work as we investigate metallic glasses at room temperature.

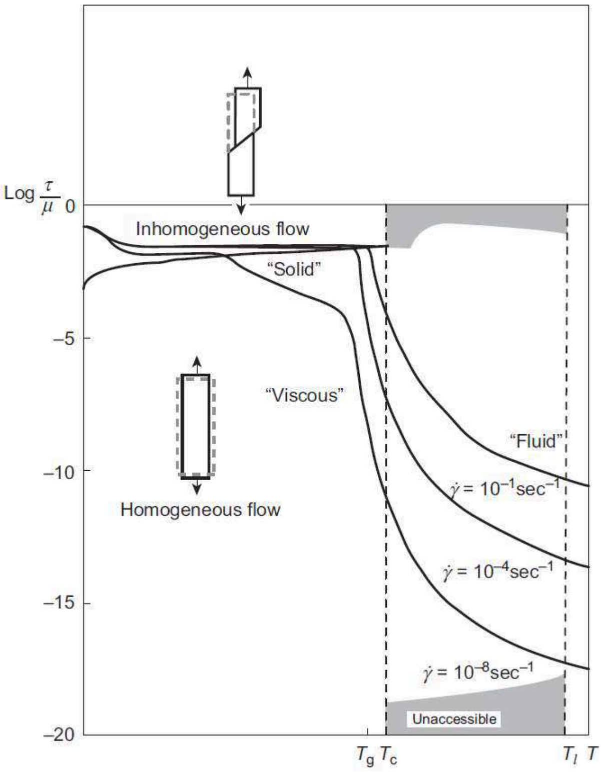

Figure 2-5: Scheme showing the different deformation mechanisms of metallic glasses in dependence of the temperature [51].

As mentioned in 2.1 no general theory has yet been developed to describe or predict mechanical properties of metallic glasses. A general correlation between Poisson's ratio ν and toughness (represented by fracture energy G_f) for metallic glasses was introduced by Lewandowski et al. [13]. The elastic constants shear modulus G and bulk modulus B are related to ν as displayed in equation [52] (1):

$$\nu = \frac{3B - 2G}{6B + 2G} \qquad (1)$$

Figure 2-6 shows the empirical results of different classes of glasses for the relationship between toughness G_f and Poisson's ratio. Lewandowski et al. concluded that a significant amount of toughness is only present for glasses which show $\nu > 0.32$. Literature data [53-56] as well as this work show that the Poisson's ratio is not a sufficient criteria to describe the brittle to ductile transition in metallic glasses. Instead, a "deeper" look into the electronic structure level is necessary. Cheng and Ma [57] give a more general view on the structure-property relationships in metallic glasses.

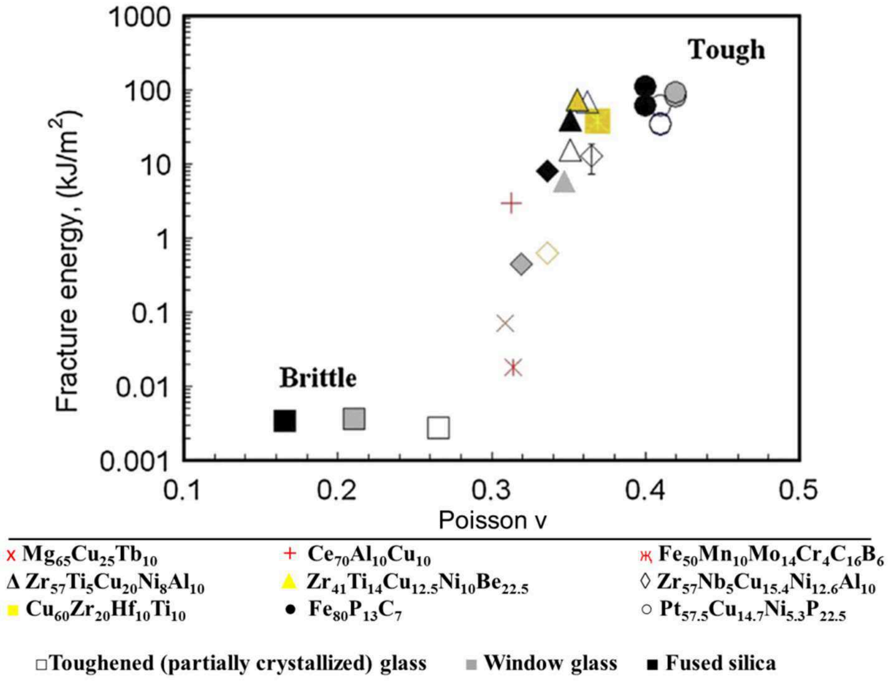

Figure 2-6: Fracture energy data of different glass types in dependence of their ν, leading to the formulation of the general brittle to tough transition rule at ν=0.32 [13].

3. Experimental methods

The applied experimental methods used during this work are described briefly. For a more detailed view on certain methods, corresponding literature is recommended in the individual subsections.

3.1 Melt spinning

Different metallic glasses were produced at MPIE by melt spinning. A (crystalline) master alloy is produced by melting elements of high purity (99.9%) in the desired stoichiometry and casting them into a cylinder. The cylinder is then processed in the melt spinner. A ribbon of 50 mm width (depending on the nozzle), 50-120 µm thickness (depending on the velocity of the copper wheel and injection pressure) and several cm length is produced by injecting the molten material onto a cooled spinning copper wheel. High cooling rates of up to 10^6 K/s are achieved by this technique resulting into amorphous ribbons [58]. The thickness of the ribbons is limited by the thermal conductivity of the alloy.

Compared to thin film sputtering, melt spinning can produce a larger volume of material (e.g. for DSC measurements).

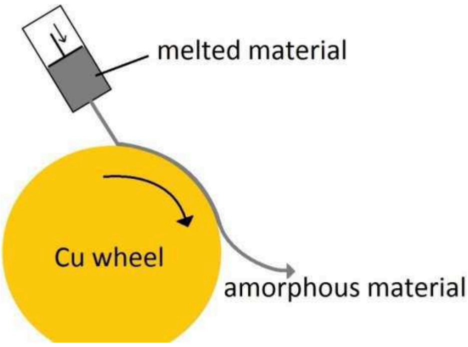

Figure 3-1: Scheme of the melt spinning process where a remolten master alloy of an individual composition is injected onto a spinning copper wheel and the high cooling rate results into amorphous ribbons of the starting material.

3.2 Thin film deposition

Different metallic glasses were produced as thin films at the Materials Chemistry department of Prof. Schneider at RWTH Aachen University by magnetron sputtering. During the sputtering process the target atoms condense on the substrate and, therefore, very high cooling rates of up to 10^{15} K/s can be achieved [59]. Up to four targets (elemental or multicomponent/compound) of 50 mm diameter and high purity are set up in a UHV chamber with an inclination angle of ≈19°. Shutters in front of the targets enables sputtering of individual elements (see Figure 3-2). The geometry allows for simultaneous or successive magnetron deposition onto the substrate. During simultaneous sputtering the desired composition of the specimen can be controlled by applying different power densities to each target. Direct current (DC) or radio frequency (RF) sputtering is used depending on the electric conductivity of the target. Ar is used as sputtering gas and optional reactive gasses (e.g. O_2, N_2) are possible candidates to assist during the sputter process. The substrate to target distance is ≈10 cm and the sputtering rates are ≈10 - 20 nm/min (depending on the target material and sputtering mode). As a substrate, Si (100) wafers of 50.8 mm diameter are used and it is possible to continuously rotate the substrate table in order to achieve a more homogenous distribution of the sputtered elements. Typically, metallic glass layers of 2-5 µm thickness have been sputtered directly onto the Si substrate or onto a preliminary sputtered adhesive Cr layer of several 100 nm. Additionally, a bias can be applied and the substrate is heatable.

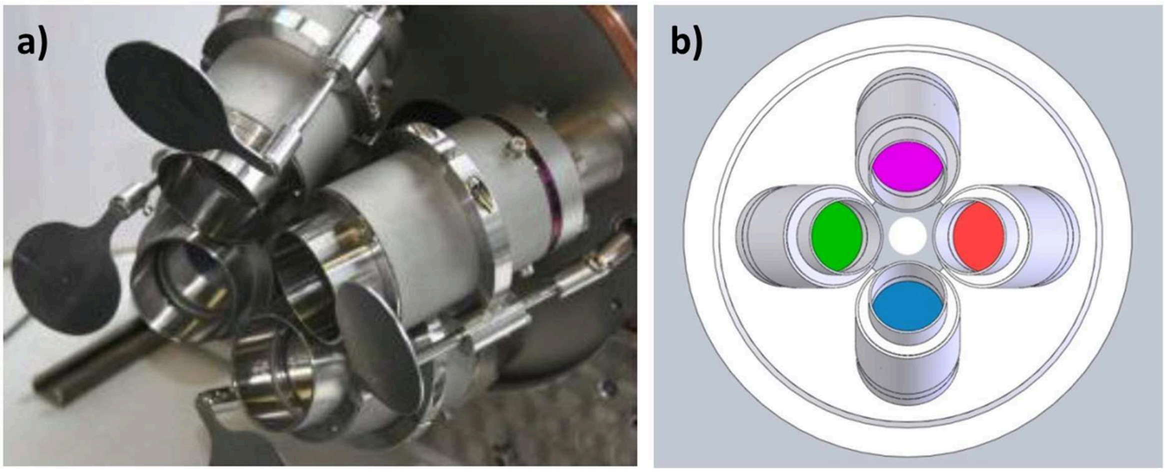

Figure 3-2: a) is showing the sputter sources with shutters as employed at RWTH Aachen University and b) shows a sketch of their geometrical arrangement.

3.2.1 Combinatorial sputtering

One drawback of the sputtering technique is that it takes a lot of time to get reasonable amounts of material. Adopting the sputter rates of ≈10 – 20 nm/min accomplishing a layer thickness of ≈5 µm takes approximately 8 hours. Adding the setup time for the sputter chamber (venting, changing targets, inserting new substrate, evacuating) it is obvious that producing multiple samples of different chemical composition within one sputtering process offers huge advantages. Therefore, the rotation of the substrate is not used on purpose and, because of the geometry of the setup, a lateral gradient in chemical composition is formed across the substrate as visible in Figure 3-3. This is due to the non-uniformly distributed flux of each plasma across the whole substrate area [60].

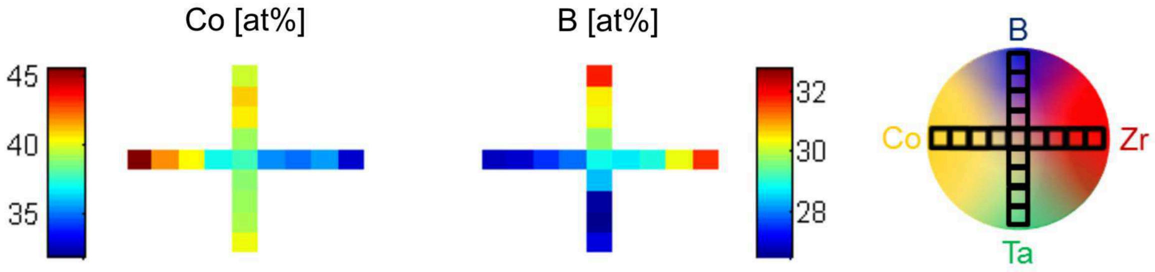

Figure 3-3: Distribution of elements (Co and B) across the deposited wafer measured by energy-dispersive X-ray spectroscopy (EDX) and map of overall concentration [61].

3.3 Nanoindentation

To compare mechanical properties such as hardness H and Young's modulus E of the produced specimen nanoindentation is used due to the small specimen dimensions. According to the method of Oliver et al. [62] a diamond tip is pushed into the flat sample surface while force and depth are recorded. To rule out substrate effects, an indentation depth of less than 10% of the film thickness is kept. The three sided pyramid geometry (face angle 65.27°) of the Berkovich indenter tip allows for an easy geometrical expression of the contact area A of indentation in dependence of the penetration depth of the indenter h_c [63]:

$$A = 3\sqrt{3}h_c^2 \tan^2 65{,}27° = 24.5h_c^2 \qquad (2)$$

The hardness H of the probed material is determined by the ratio of the maximum load P_{max} and contact area A [63]:

$$H = \frac{P_{max}}{A} = \frac{P_{max}}{24.5h_c^2} \tag{3}$$

The reduced Young's modulus E_r can be determined by the slope dP/dh of the load-displacement curve during unloading as described in equation (4) [63]:

$$E_r = \frac{\sqrt{\pi}}{2\sqrt{A}} \frac{dP}{dh} \tag{4}$$

The relationship between the Young's modulus of the probed sample E_s and the reduced Young's modulus E_r can be calculated if the Young's modulus of the Indenter E_i and the Poisson's ratios v_i of the indenter and v_s of the sample are known:

$$\frac{1}{E_r} = \frac{1 - v_i^2}{E_i} + \frac{1 - v_s^2}{E_s} \tag{5}$$

3.4 Micro cantilever bending tests

As mentioned in section 3.2 thin film sputtering enables better control of the homogeneity and composition of the samples. The in 3.2.1 described preparation of combinatorial thin films allows efficient testing of multiple compositions. Due to the limited dimensions it is not possible to perform conventional macroscopic tensile tests in order to determine mechanical properties. Micro cantilever bending tests (see Figure 3-4) of FIB-machined specimen were tested according to the method described by Matoy et al. [64] (brittle case) and Wurster et al. [65] (ductile case) which allows for investigations of the mechanical properties of thin films. It has been shown by Balila et al. [66] that the obtained data is comparable to bulk data. The fracture strength σ was determined by deforming un-notched cantilevers, while the fracture toughness (K_{IC}) was measured on notched ones.

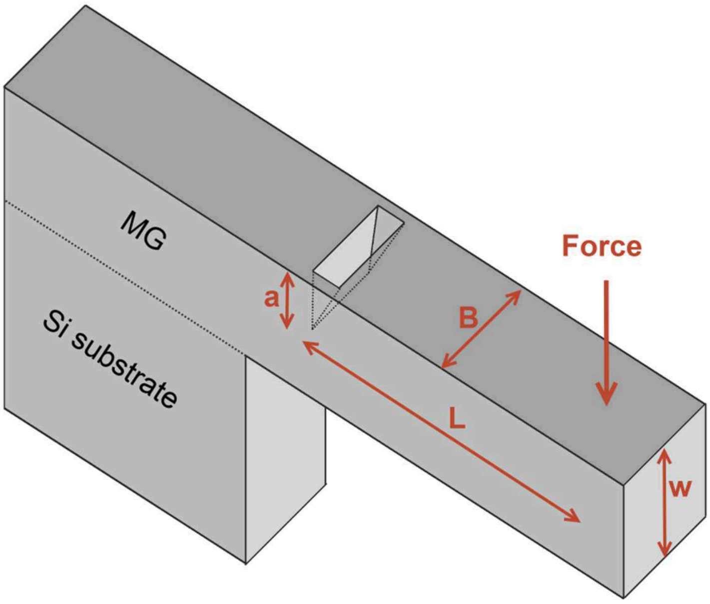

Figure 3-4: *The sketch shows an exemplary cantilever with bending length L, notch depth a, width B and thickness w. The bending direction and position of indenter contact area are indicated.*

3.4.1 Analytical formula for fracture toughness/strength

In the case of brittle fracture, the toughness K_{IC} of the samples has been calculated by linear elastic fracture mechanics (LEFM), using the maximum applied load F_{max}, length L, width B, thickness w and notch depth a of the cantilevers in equation (6):

$$K_{IC} = \frac{F_{max}\, L}{B\, w^{\frac{3}{2}}}\, f\left(\frac{a}{w}\right) \qquad (6)$$

The function *f(a/w)* is the shape factor and is determined by Matoy et al. [64] using FEM simulation in ABAQUS. It is important to notice that an isotropic material model is used, which is only valid for amorphous materials. For bridged notches in single cantilever beams *f(a/w)* is given as:

$$f\left(\frac{a}{w}\right) = 1{,}46 + 24{,}36\left(\frac{a}{w}\right) - 47{,}21\left(\frac{a}{w}\right)^2 + 75{,}18\left(\frac{a}{w}\right)^3 \qquad (7)$$

Micro cantilever bending tests

For the ductile case it is possible to determine the fracture toughness by using J-integrals which contain an elastic part (first term) and a plastic part (second term):

$$J_{(i)} = \frac{K_{(i)}^2(1-\nu^2)}{E} + \frac{\eta A_{Pl(i)}}{B(w-a_0)} \qquad (8)$$

$K_{(i)}$ is given by equation (6), η =2 is a constant factor, ν is the Poisson's ratio, E is the Young's modulu and $A_{Pl(i)}$ is the area beneath the load-displacement curve.

In order to calculate the J-integrals, it is necessary to know the evolution of the crack during the experiment. According to Wurster et al. [65] the crack growth can be determined by *in situ* observation of the crack growth in the scanning electron microscope (SEM), or by the unloading compliance of the cantilever after each cycle. Due to the poor resolution of the used SEM, the unloading compliance *k* is used to determine the crack growth.

$$w - a_i = \sqrt[3]{\frac{4kL^3}{BE}} \qquad (9)$$

The fracture toughness $K_{I,C}$ is calculated using the maximum $J_{I,C}$:

$$K_{I,C} = \sqrt{\frac{J_{I,C}E}{1-\nu^2}} \qquad (10)$$

The strain energy release rate or fracture energy G_f is calculated using the K_{IC} or J_{IC} values of the individual metallic glass thin films.

$$G_f = J_{IC} = \frac{{K_{IC}}^2(1-\nu^2)}{E} \qquad (11)$$

To calculate the fracture strength σ of the un-notched cantilevers the formula given by linear-elastic bending theory is used:

$$\sigma = 6\,\frac{F_{max}\,l}{B\,w^2} \qquad (12)$$

3.4.2 Sample preparation by focused ion beam (FIB) and chemical etching

For the micro cantilever bending tests free standing metallic glass films are required. In order to reduce the preparation time and to prevent expendable beam damage induced by the FIB, the Si substrate underneath the metallic glass thin film is partially etched at 70 °C by 30% KOH solution for 45 minutes [67]. Figure 3-5 a) shows a schematic view of the etching process which results in an overhanging metallic glass layer. Afterwards, a coarse mask of the cantilevers is FIB-machined into the surface using high currents (30 kV, 2.5 nA). The cantilevers' shape is refined by additional milling steps (30 kV, 0.28 nA, dimensions: 18 µm × 2.5 µm × 2.5 µm). For the notched samples a bridge-notch of 100 nm width and a depth of approximately 30% of the film thickness is milled (30 kV, 7.4 pA) into the cantilever. In a final step, the individual dimensions of each cantilever are extracted by analyzing the recorded SEM images (see Figure 3-5 b)) and used as input parameters for the calculations.

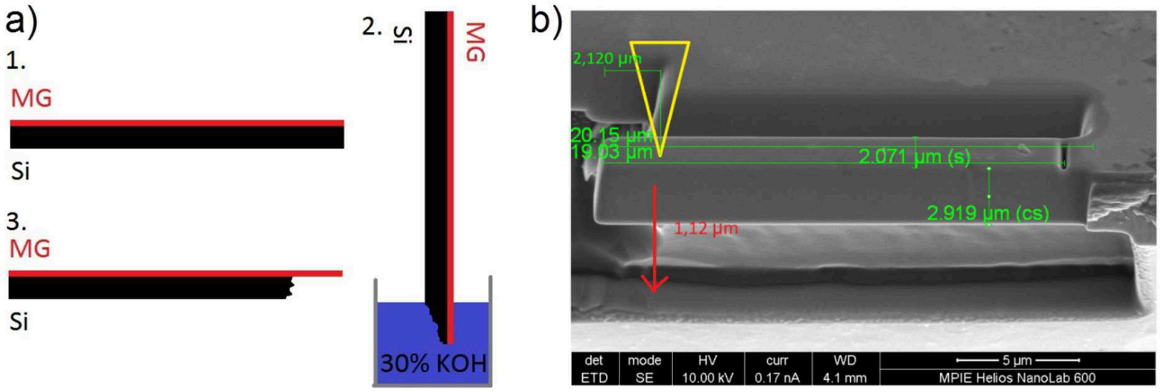

Figure 3-5: a) Sketch of the partial etching process showing the free standing metallic glass layer. b) SEM image of a ready to test notched CoZr metallic glass cantilever showing the dimensions and position of the indenter.

3.4.3 Bending of micro cantilever beams

The prepared samples are transferred to the *in situ* SEM indentation system (ASMEC UNAT-2). The positioning of the conical indenter (1 µm tip radius) at the tip of each cantilever is done manually via the SEM images, which allows to determine the exact bending length. The indenter is operated in a displacement controlled mode and the load-displacement curves of the bending experiments are recorded. SEM images are taken before and after the experiments to determine the actual bending length. The whole bending experiment is recorded by the SEM to allow for error analysis, such as gliding or slipping of the indenter. After the bending experiment, each cantilever is imaged by SEM for additional investigations of the fracture surface and the actual notch depth is measured.

3.5 Atom Probe Tomography (APT)

Atom Probe Tomography (APT) is a chemically sensitive, three-dimensional, destructive characterisation technique to investigate elemental distributions of small probe volumes (several million atoms) [68] with near atomic resolution [69], which was first introduced by Erwin Müller in 1967 [70]. The specimen atoms are ionized and field evaporated towards a position sensitive detector and reconstructed in a 3D computer model (see Figure 3-7).

3.5.1 Basic principles of APT

An APT can be described as a combination of a field ion microscope [71] and a mass spectrometer [69]. A needle-shaped specimen (R <100 nm) is placed into a ultra-high vacuum chamber ($\approx 10^{-11}$ mbar) and cooled to temperatures of 10 – 90 K [68] to prevent surface diffusion. A high “base” potential U_{DC} is applied between the specimen and the counter electrode. The electric field F at the tip of the specimen can be calculated using the applied voltage U, the field factor k_f which depends on the tip shape and the tip radius R as given in equation (13):

$$F = \frac{U}{k_f R} \qquad (13)$$

An electric field F of 30 - 50 V/nm [69] at the tip is necessary to field evaporate ions depending on the element. Therefore, the voltage is overlaid by an additional pulsed voltage (voltage mode) or laser pulse (laser mode) to overcome the potential barrier *Q(F)* (see Figure 3-6) and field evaporate the surface atoms from the specimen towards the detector.

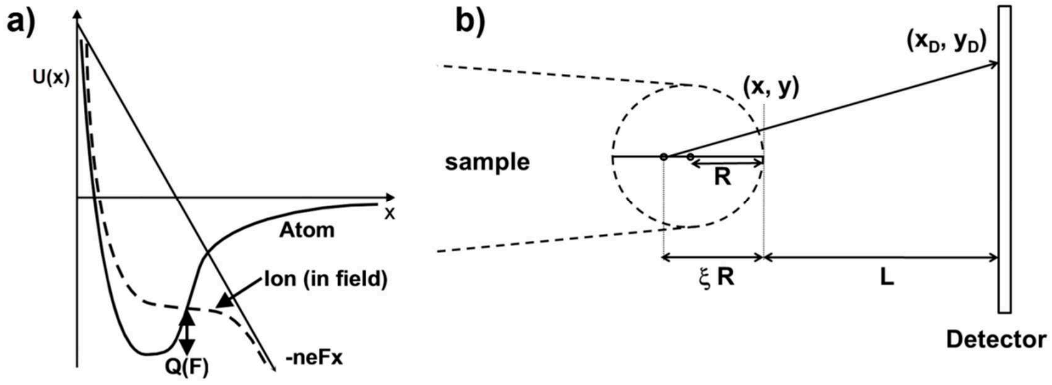

Figure 3-6: a) Atomic and ionic potential energy diagram with electric field [69] b) Schematic view of the point-projection [72].

To identify the chemical species of the ions the time of flight t between the pulse and the detection on the detector is measured for each individual ion. The mass m to charge n ratio is calculated using the fact that the kinetic energy of the ions is equal to their potential energy. The potential U contains out of the "base" potential U_{DC} and the pulsed potential U_P:

$$\frac{1}{2}mv^2 = neU \qquad (14)$$

The velocity v of the ions can be expressed by the flight length L and the time of flight t to:

$$v = \frac{L}{t} \qquad (15)$$

This results into the following expression for the mass to charge ratio:

$$\frac{m}{n} = 2eU\left(\frac{t}{L}\right)^2 \qquad (16)$$

To derive the original x and y coordinates of the atom within the specimen, a position sensitive detector is used and the coordinates on the detector X_D and Y_D are reverse projected onto the tip according to the point-projection model [72]. The magnification *M* is given by equation (17) using the image compression factor which corrects for the compression of field lines towards the centre and tip radius *R* (see Figure 3-6 b)):

$$M = \frac{L}{\xi R} \tag{17}$$

$$x = \frac{X_D}{M}, y = \frac{Y_D}{M} \tag{18}$$

The *z* coordinate of the ions is identified by the evaporation sequence. The z_i position of the *i*th ion is calculated by summing up the depth increments *dz* and adding the correction factor *dz′* which accounts for the evolving curvature of the sample [73]:

$$dz = \frac{\Omega}{\xi S_A} \tag{19}$$

$$dz' = R\left(1 - \sqrt{1 - \frac{x^2 + y^2}{R^2}}\right) \tag{20}$$

$$z_i = \left(\sum_{1}^{i} dz\right) + dz'_i \tag{21}$$

Where Ω is the average atomic volume and S_A is the analysed area. The radius *R* is evolving (blunting) during the measurement and the evolution of *R* in dependence of the evaporation sequence needs to be considered for a correct reconstruction. The acquired data sets are reconstructed and analysed in the IVAS 3.6.10 (CAMECA instruments) software [68], which uses an evolved algorithm for the determination of *z*, which induces less distortions towards the edges of the field of view [74, 75]. Voltage reconstruction, shank-angle reconstruction, and tip profile reconstruction are the available methods within the IVAS software to account for *R(z)* [72].

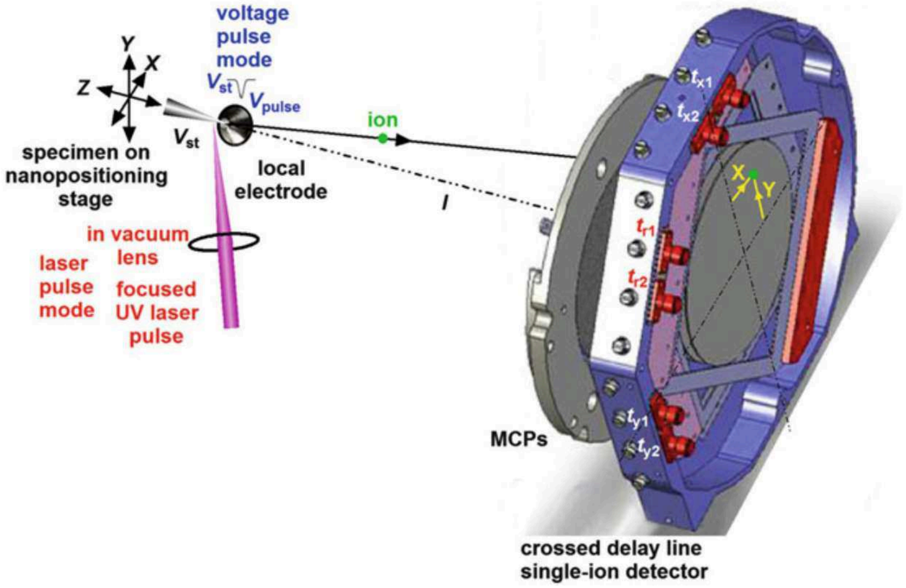

Figure 3-7: Principle of APT [76] showing the tip shaped sample, local electrode and position sensitive detector.

3.5.2 Field evaporation of amorphous materials

In contrast to crystalline material the bonds between the individual atoms of an amorphous material are not well defined. Because of this some problems emerge for the reconstruction of field evaporated amorphous specimen.

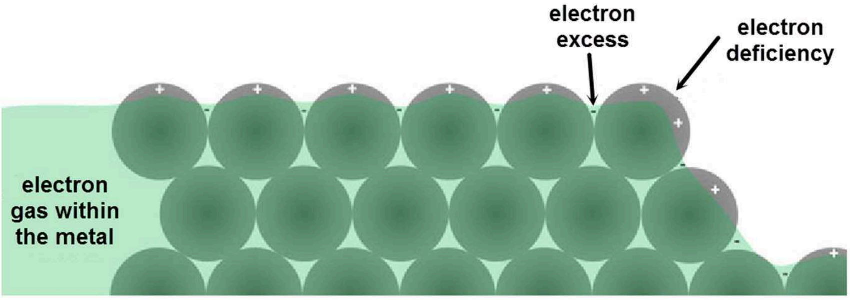

Figure 3-8: Surface of a positively charged crystalline metal [72].

The terrace like evaporation of ions which are exposed to a high electric field is a fundamental assumption for the reconstruction of the *z* coordinate [72]. Figure 3-8 shows that this is true for crystalline metals where protruding atoms are favoured in evaporation because the surrounding electric field is higher. Additionally, the “corner” atoms along the terraces of the atomic planes are exposed to fewer bonds of the surrounding atoms. This results into the preferential evaporation of “corner” atoms and supports the sequential evaporation process out of which the z coordinate of the ions is reconstructed. This is not possible for amorphous metals. According to Müller [77] the activation barrier for field evaporation *Q(F)* of crystalline metals is given by equation (22):

$$Q(F) = \Lambda + \sum_{i=1}^{n} I_i - n\Phi_e - \sqrt{\frac{n^3 e^3 F}{4\pi\varepsilon_0}} \qquad (22)$$

Where Λ is the binding energy of the surface atom, I_i is the ionization energy and Φ_e is the electron work function. Equation (23) expresses the evaporation rate ϕ_{evap} :

$$\phi_{evap} = v_o exp\left(-\frac{Q(F)}{k_B T}\right) \qquad (23)$$

Unfortunately, no such expressions exist for amorphous metals. The binding energy Λ in equation (22) is not well defined for atoms in an amorphous material, which results into an inhomogeneous evaporation rate (see equation (23)). The whole evaporation process in amorphous materials is not fully understood and no theory exists to describe a correct reconstruction algorithm of amorphous materials. The assumption of layer-by-layer evaporation, which results into correct *z* coordinates, fails in the case of amorphous materials. Instead of the homogenous unzipping terraces of atoms the amorphous materials’ evaporation is described as an inhomogeneous “boiling surface” evaporation [78]. This yields a loss in *z* accuracy. The *x* and *y* coordinates are also slightly affected because the inhomogeneous evaporation leads to differing field intensities. This causes changes in the specimen geometry [79, 80] which results into a change in the trajectories of the ions [81].

Additional problems may occur because the evaporation of an atom destabilises the surrounding atoms, which can cause preferential evaporation around this “hot spot” and lead to local magnification effects [82].

Although current reconstruction algorithms are not explicitly based on field evaporation models for amorphous materials, they show reasonable results for most applications. Nevertheless, it is important to know about the limitations of APT especially for amorphous materials. Methods which are based on very exact atom positions with low scatter (e.g. radial distribution functions (RDF)) should not be applied to amorphous materials [78, 83].

3.5.3 Frequency distribution analysis of elemental occurrence

For further analysis, the 3D-reconstructed APT data is partitioned into a mesh of voxels or blocks (see Figure 3-9). This is done either by keeping the number of atoms per block n_b constant (population voxelisation) or keeping the dimensions x, y, z of the blocks constant (volume voxelisation).

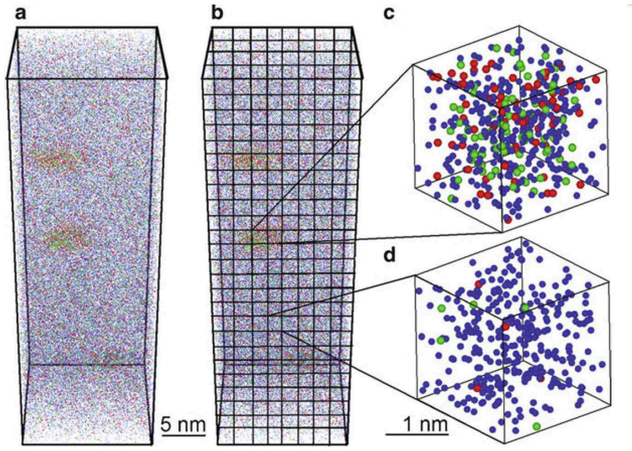

Figure 3-9: Al-Mg-Zn atom probe reconstruction showing the principle of voxelisation into blocks of equal size (number of atoms) [72].

The frequency of each atomic species per block is recorded for all blocks, which results into a frequency distribution for each individual element. The distribution is visualised showing the frequency of blocks, which contain a certain number of atoms n of an individual species A. In a completely random sample with no inner structure this yields a binomial distribution which can be expressed as [84]:

$$f_b(n) = NP_b(n) = N\frac{n_b!}{n!\,(n_b - b)!}X_A^n(1 - X_A)^{(n_b - n)} \qquad (24)$$

Where n_b is the total number of atoms per block, *N* signifies the total number of blocks, X_A stands for the proportion of *A* atoms, $P_b(n)$ is the binomial probability distribution and $f_b(n)$ is the expected number of blocks containing *n* atoms of element *A*. By comparing the theoretical frequency distributions, $f_b(n)$ in equation (24), with those observed experimentally, *e(n)*, it is possible to retrieve information about the inner structure of the investigated sample. Any deviation or shift between the two distributions indicates a non-randomness of atoms in the sample (e.g. crystallographic order, decomposition, clustering). The degree of deviation can be quantified by χ^2 as displayed in equation (25) [85]:

Atom Probe Tomography (APT)

$$\chi^2 = \sum_{n=0}^{n_b} \frac{(e(n) - f_b(n))^2}{f_b(n)} \tag{25}$$

To minimize the influence of different block sizes the Pearson coefficient μ has been introduced using the number of blocks sampled N_S for standardization reasons [85]:

$$\mu = \sqrt{\frac{\chi^2}{N_S + \chi^2}} \tag{26}$$

3.5.4 APT specimen preparation by FIB

The specimen preparation for APT is performed using a FEI Helios Nanolab 600i dual-beam focused ion beam (FIB) equipped with a micro-manipulator. A conventional site-specific lift out procedure according to Thompson et al. [86] is employed to prepare sharp tips (r <100 nm) out of the region of interest. First, a protective Pt- layer is deposited (30 kV, 0.23 nA) onto the surface of the sample to prevent Ga damage during the fibbing process. In a second step, the triangular shaped beam is cut free using the ion beam (30 kV, 9.3 nA) to undercut the region of interest which is just attached at one side (see Figure 3-10). The micromanipulator needle is Pt-welded (30 kV, 40 pA) onto the triangular shaped beam which is then cut completely free and lifted out of the sample surface. In a next step, the attached specimen is transferred onto a pre sharpened tip, a grid of 6x6 pre-sharpened, flat-top Si posts or a pre-sharpened TEM-grid for correlative APT/TEM measurements (see 3.7), and Pt-welded. The last step is to sharpen the specimen using annular ion beam milling (decreasing energy 30 kV, 0.79 nA -> 0.23 nA -> 80 pA) where the final step is performed at low energy (5 kV, 41 pA) to prevent Ga damage. The final form of the tip (radius, shank angle) is documented by SEM images as input for the reconstruction. Applying the described technique, it is possible to prepare up to eight APT tips out of one triangular shaped beam which increases throughput of APT experiments.

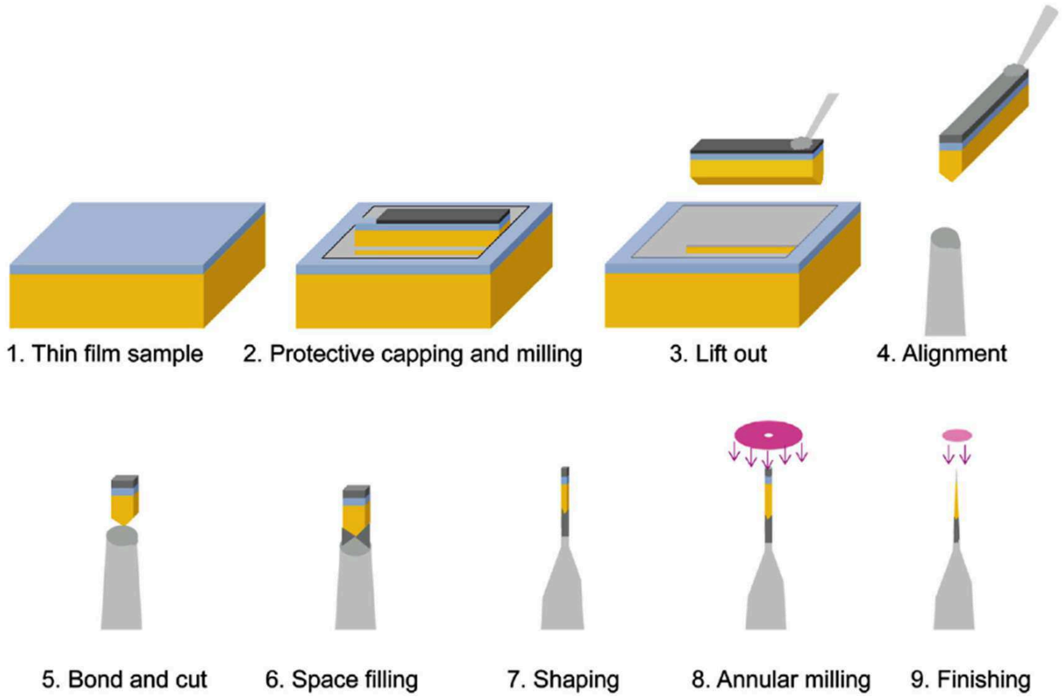

Figure 3-10: Sketch of the APT sample preparation method based on [87]. 1-3 show the lift out of the region of interest from the material which is mounted onto a pre manufactured silicon tip (4-6). 7-9 show the final sharpening process of the APT tips.

3.6 Scanning transmission electron microscopy (STEM)

Scanning transmission electron microscopy (STEM) is a well-established technique for analyzing microstructure and composition of various materials. It is a special form of the transmission electron microscopy (TEM). Different STEM operation modes and related techniques are employed during this work and discussed briefly.

Electrons are emitted and accelerated towards a thin sample (thickness <100 nm) where they interact with the atoms of the specimen. Different detectors record different interactions of the transmitted electrons (see Figure 3-11).

Scanning transmission electron microscopy (STEM)

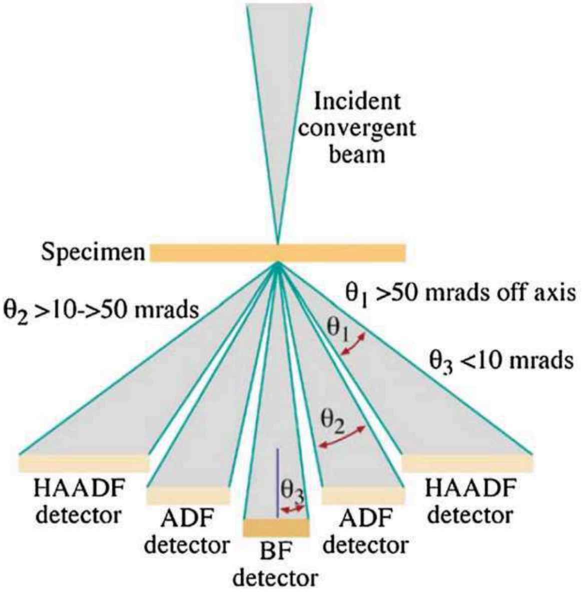

Figure 3-11: Sketch from Williams and Carter's TEM book showing the different electron detectors of a STEM [88].

3.6.1 Recording diffraction patterns in STEM

An advantage of STEM diffraction patterns compared to XRD diffraction patterns is their much shorter wavelength λ and the significantly smaller spot size (≈2 nm). The wavelength of the electrons can be expressed by the relativistic corrected de Broglie relationship [89] using Planck's constant *h*, the rest mass of the electron m_0, the accelerating voltage of the gun *V* and the charge of the electron *e*.

$$\lambda = \frac{h}{\sqrt{2m_0 eV \frac{1+eV}{2m_0c^2}}} \tag{27}$$

According to equation (27) a wavelength of λ =3.7 pm is achieved for a 100 kV TEM, while the atomic spacing is in the order of Å (100 pm). Because of the small spot size much smaller objects, such as nanocrystals or single grains, can be probed without getting any intensity from the rest of the sample. The electrons are elastically scattered at the atoms of the sample and in a crystalline material characteristic diffraction patterns are formed depending on the crystallographic orientation [90].

Amorphous materials, such as metallic glasses, show diffuse rings because due to the lack of lattice planes no constructive interference is possible. Therefore, it is easy to distinguish between diffraction patterns of amorphous or crystalline materials (see Figure 3-12).

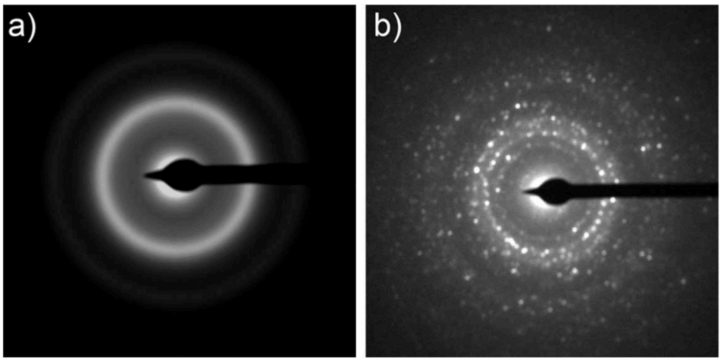

Figure 3-12: STEM diffraction patterns of a $Co_{44}Fe_{24}Y_5B_{27}$ *metallic glass sample showing the difference between the diffuse rings of an amorphous as prepared state a) and in the partially crystalline state after annealing to 650°C for 5 minutes in b).*

3.6.2 Bright field / dark field imaging in STEM

For the bright field (BF) and (annular) dark field ((A)DF) imaging the TEM is operated in scanning mode (STEM). A convergent focused electron beam is used to scan the sample and depending on the angle in which the scattered electrons are detected (Figure 3-11) a BF or DF image is recorded.

The BF detector is positioned on the optical axis of the microscope and only electrons that are scattered in very small angels (ϑ_3 in Figure 3-11) and primary electrons are recorded. The loss of primary electrons due to absorption or scatter at the sample is the responsible mechanism for the imaging. By BF imaging a mass-thickness and diffraction contrast is achieved. Thick areas and areas where heavy elements are distributed appear dark in the BF mode.

For the DF or ADF detector, the primary electron beam is explicitly not recorded. Thus, only scattered electrons under and angle of ϑ_2 (Figure 3-11) contribute to the image. These scattered electrons contain Bragg diffracted electrons and elastically scattered electrons (Rutherford scattering see 3.6.3). Hence, a DF image provides crystallographic contrast (Bragg) as well as Z-contrast Rutherford [91]. The ratio of Bragg- and Rutherford scattered electrons can be adjusted by the camera length.

3.6.3 Mapping samples in STEM by High-angle annular dark field (HAADF)

In order to reduce the amount of Bragg scattered electrons a HAADF detector is located even further away from the optical axis (θ_1 in Figure 3-11) than the (A)DF detector. The advantage of the HAADF-STEM mode is the direct link between the image intensity and the atomic number because only Rutherford scattered electrons reach the detector. The intensity is proportional to Z^2 (28) and, consequently, regions with high atomic number appear bright, while regions with low atomic number appear dark. Because of this behaviour HAADF-STEM images are also called "Z-contrast images". This incoherent Rutherford scattering is described by using the differential cross-section $d\sigma/d\Omega$, scattering angel $\boldsymbol{\Theta}$ and the atomic number Z [88].

$$\frac{d\sigma}{d\Omega} = \frac{Z^2 e^4}{16 E_0^2 sin^4 \Theta} \qquad (28)$$

Our partners within the SPP-1594 of the University of Münster developed a method to determine relative density changes of shear bands ρ_{SB} and matrix ρ_M directly from the intensity changes I of the HAADF-STEM signal [5, 92]:

$$\Delta\rho = \frac{\rho_{SB} - \rho_M}{\rho_M} = \frac{I_{SB} - I_M}{I_M} \qquad (29)$$

Thus, it is possible to visualise chemical fluctuations of shear bands in metallic glasses compared to the matrix by HAADF-STEM measurements. In order to detect mostly electrons which are scattered far away from the optical axis and therefore minimize the contribution of only Bragg scattered electrons, a short a camera length is applied.

3.6.4 TEM lamella sample preparation

The site-specific lift-out procedure for the TEM lamella is performed according to the method described in the review of Giannuzzi et al. [93]. Like the lift out for the APT specimens (see 3.5.4), a FEI Helios Nanolab 600i dual-beam focused ion beam (FIB) equipped with a micro manipulator is used to deposit a protective Pt-layer onto the region of interest (30 kV, 0.23 nA) to prevent Ga damage during the thinning process (see Figure 3-13). Trenches are milled (30 kV, 9.3 nA) into the surface by focused ion beam and an undercut is performed to cut the lamella free, which is now only attached to one side. The micromanipulator is Pt-welded (30 kV, 40 pA) to the lamella, which is finally cut free completely and lifted out of the surface. The lamella is transferred to a pre-manufactured Cu-grid and Pt-welded onto one of the posts. In a final step, the lamella is thinned down to ≈50nm by applying a cleaning cross section milling (decreasing energy 30 kV, 0.43 nA -> 80 pA) from the top. The final milling steps are performed at low energy (5 kV, 41 pA) to prevent Ga damage [94].

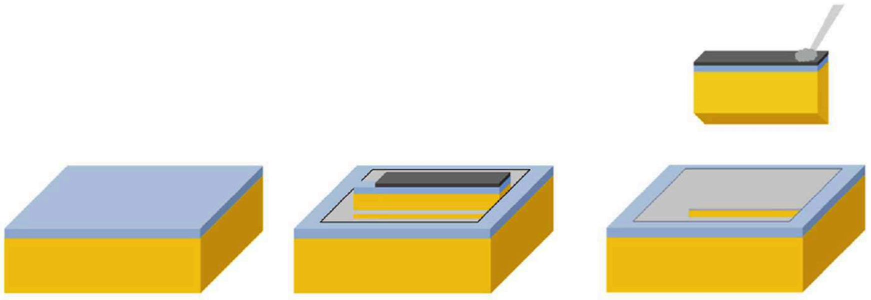

1. Thin film sample 2. Protective capping and milling 3. Lift out

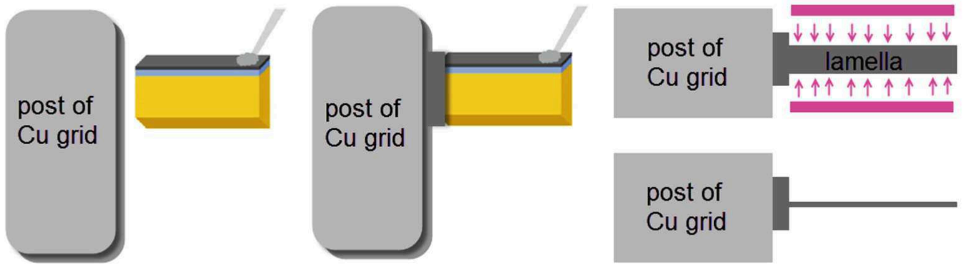

4. Approach and Alignment 5. Pt-welding 6. Top view of thinning process

Figure 3-13: Scheme of TEM lamella preparation by FIB. 1-3 shows the lift out of the region of interest, while 4-5 visualize the mounting of the TEM lamella onto a pre manufactured TEM grid. 6 shows the final thinning process of the TEM lamella.

3.7 Correlative investigations (TEM/APT)

For the correlative TEM/APT measurements the setup developed by Herbig et al. [95] has been used. The APT tips have been lifted out and mounted onto a pre-cut and electropolished TEM grid according to 3.5.4. Special holders for the TEM and APT allow for an easy transfer between the two instruments. Therefore, it is possible to image and characterise the ready-to-measure APT specimens in the TEM. After the APT experiment the specimens are again imaged in the TEM to increase the accuracy of the reconstructions. The reconstructed APT data set and the TEM images can be overlaid which allows to combine the advantages of both methods (see Figure 3-14). Consequently, additional information can be drawn from the analysed sample. In this work the positions and density variations of shear bands are examined by TEM and correlated with APT data which resolves their chemical composition.

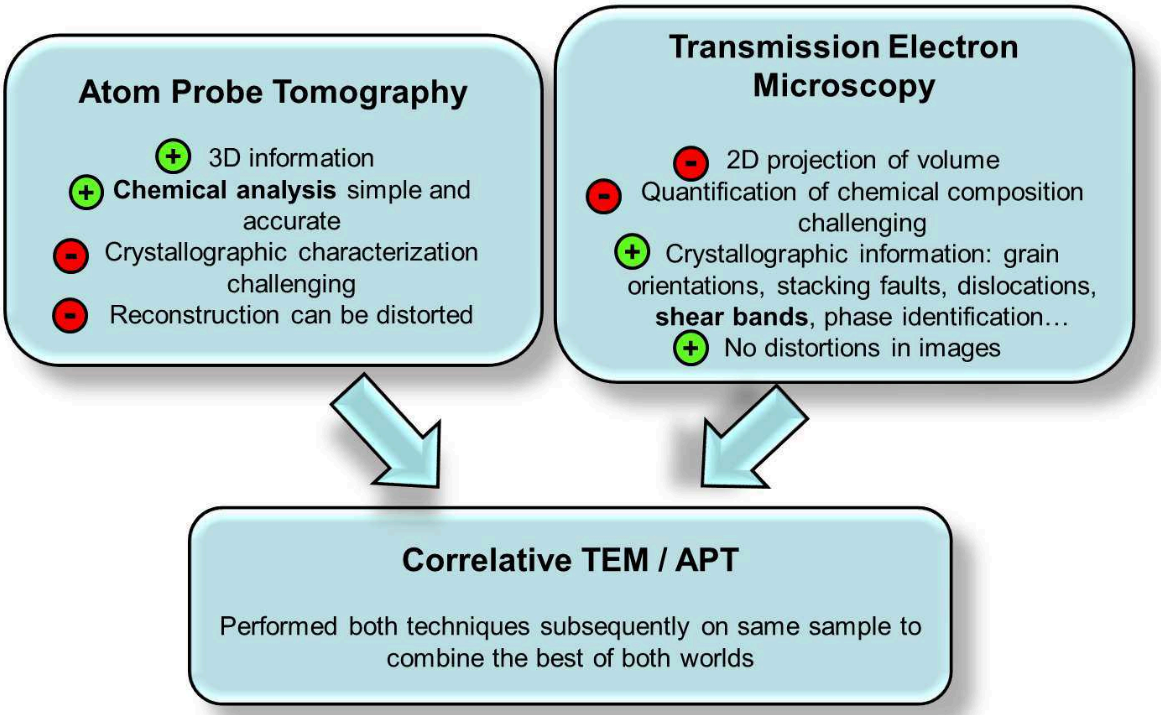

Figure 3-14: Drawbacks and advantages of APT/TEM according to Herbig [95].

3.7.1 TEM/APT tip sample preparation by FIB

For the correlative TEM/APT measurements, specimens are prepared from bent cantilevers. Figure 3-15 shows the heavily deformed region around the notch of the cantilever contains a lot of shear bands. The visible shear steps at the surface of the material are marked with red arrows and they are the only indicators for the positions of shear bands. After the first milling steps the position and evolution of an individual shear band is unknown. In order to improve the chances of preparing an APT specimen that contains a shear band within the first 500nm, only regions with high shear band density are picked and therefore a limited amount of specimens (≈2) can be prepared from one cantilever. The cross-section of the in 3.4.2 prepared cantilevers are of rectangular shape and in order to Pt-weld them onto the pre-sharpened TEM grid as explained in 3.5.4 a triangular shaped beam is necessary as seen in Figure 3-10. Therefore, the region of the cantilever which is later Pt-welded is shaped accordingly by using a FEI Helios Nanolab 600i dual-beam focused ion beam (FIB) equipped with a micro manipulator. The manipulator is Pt-welded to the cantilever and moderate FIB currents of 0.48nA at 30kV are used to cut the cantilever free. The rest of the procedure is similar to what is described in 3.5.4.

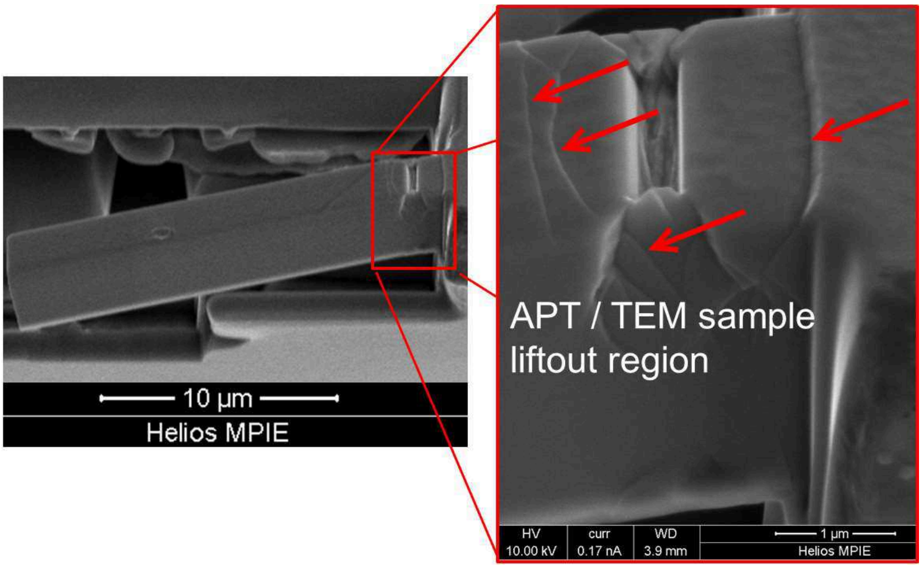

Figure 3-15: SEM images of a deformed pre-notched cantilever showing the region with high shear band density and the shear steps at the surface indicated by the red arrows before the lift out.

4. Selected compositions and their structural characterisation

The outcome of different alloying strategies in terms of mechanical properties has been tested by MD simulations in order to pick promising MG candidates. The best performing compositions were produced by magnetron sputtering or melt spinning, followed by investigating their homogeneity and amorphousness.

4.1 Promising metallic glass candidates from MD simulations

The group of Prof. Schneider at RWTH Aachen University used MD simulations in order to test three different alloying strategies, which were inspired by literature data [40, 96]. It is suggested that strong covalent (Co,Fe)-B bonds increase the stiffness of Co-based MGs [36].

"The first computational strategy focuses on systematically varying the valence electron concentration and size by substituting Fe with transition metals namely Y, Zr, Nb, Mo, Hf and W. The second computational strategy focuses on systematically investigating the metal to non-metal interactions by substituting B with other non-metals namely C, N and O. The third computational strategy focuses on the influence of non-metal concentration by increase the B content up to 50 at% by substituting Fe." [97]

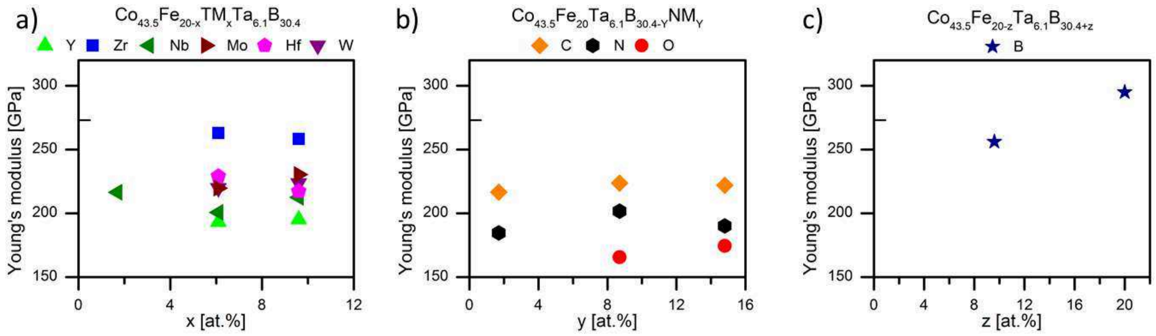

Figure 4-1: Ab initio calculated Young's modulus for the three alloying strategies in dependence of the chemical composition x,y,z. a) shows the influence of the valence electron concentration by substituting Fe with transition metals TM. b) indicates the effect of metal to non-metal NM bonds by substituting B with NM. c) visualizes the variations of Young's modulus for the substitution of Fe with B in order to increase the non-metal concentration [97].

4.2 Characterisation of samples as prepared by melt spinning/magnetron sputtering

The main focus of this work is to improve and understand the mechanical properties and their underlying mechanisms in metallic glasses. Therefore, it is of great importance and interest to have fundamental/sound knowledge of the initial configuration and condition of the produced specimen. A number of different experiments, such as X-ray diffraction (XRD), transmission electron microscopy (TEM), differential scanning calorimetry (DSC) and atom probe tomography (APT), were performed to gather structural information about the specimen as prepared by melt spinning or magnetron sputtering. Exemplary results for each technique are shown, while all compositions have been tested accordingly. It is essential to ensure only homogenous, amorphous materials were investigated to exclude any side effects of crystallisation, clustering, segregation, decomposition or others during the characterisation of the mechanical properties.

4.2.1 X-ray diffraction (XRD) patterns of exemplary metallic glasses

In order to proof the amorphous state of the prepared samples, XRD patterns are recorded using a standard θ - 2θ setup (GE Seifert Theta - 2 Theta, Cobalt λ =0.178897 nm). The random distribution of atoms in metallic glasses (see 2.1) results into the absence of sharp, well defined Bragg peaks because the Bragg condition can never be fulfilled [98]. This absence and the characteristic broad peaks can be used to proof the amorphous state of the prepared samples.

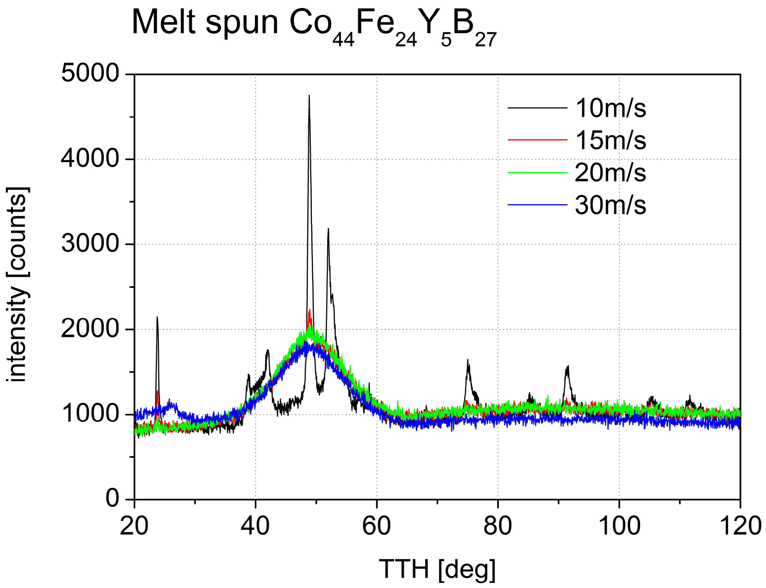

Figure 4-2: *XRD pattern of melt spun* $Co_{44}Fe_{24}Y_5B_{27}$ *metallic glass sample showing the effect of different wheel speeds (cooling rates) during melt spinning.*

Figure 4-2 shows the importance of controlling and monitoring the experimental parameters of the melt spinning process. The speed of the Cu-wheel is inversely proportional to the thickness of the ribbons and, thus, effects the cooling rate (see section 3.1). The samples produced on the fast spinning wheel (20 m/s and 30 m/s) show an amorphous XRD pattern. In contrast, the samples produced on the slow spinning wheel (10 m/s and 15 m/s) show sharp Bragg peaks and, therefore, contain crystals. The amorphous state is also proofed for the sputtered thin film samples. According to 3.1 the cooling rates of the sputtering technique are orders of magnitude faster than the ones of the melt spinning process. Figure 4-3 shows examples of amorphous Co-based metallic glasses for different compositions. The two visible peaks are due to substrate effects and the underlying Cr-adhesion layer.

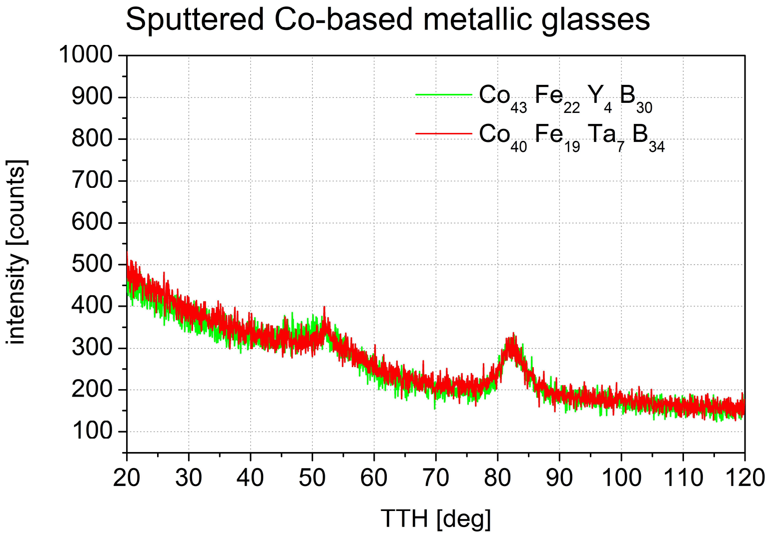

Figure 4-3: XRD patterns of sputtered Co-based metallic glasses showing their amorphous as prepared state. The two visible peaks correspond to the underlying Si substrate.

4.2.2 Transmission electron microscopy (TEM)

TEM lamellas of sputtered and melt spun metallic glass compositions have been prepared according to 3.6.4. To prove the amorphous state of the as prepared samples selected area diffraction (SAD) patterns are recorded using a Philips CM20 TEM. Figure 4-4 shows an example of a $Pd_{57}Cu_{11}Al_{24}Y_8$ metallic glass thin film, which has been probed at several spots. The substrate Si shows the characteristic diffraction pattern of a crystalline material. In comparison, the diffuse rings reflect the typical TEM diffraction patterns of amorphous materials (see section 3.6.1). All regions of the metallic glass layer in Figure 4-4 show amorphous diffraction patterns.

Characterisation of samples as prepared by melt spinning/magnetron sputtering

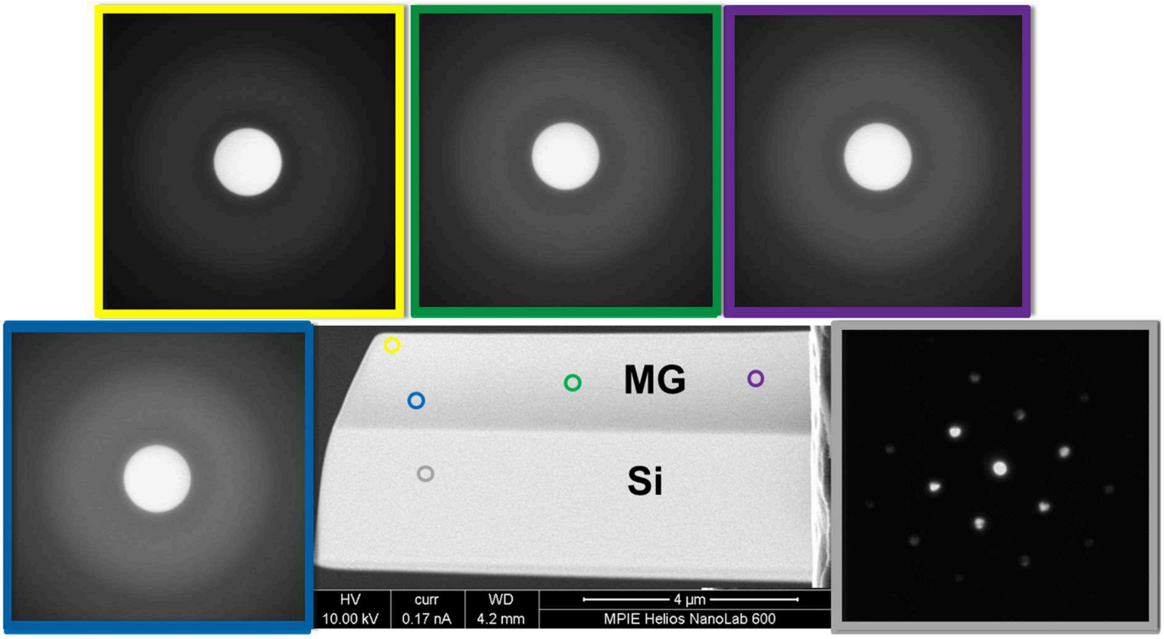

Figure 4-4: *SEM image overview and (SAD) TEM diffraction patterns of different positions along a* $Pd_{57}Cu_{11}Al_{24}Y_8$ *thin film lamella.*

Recording TEM diffraction patterns is important to exclude the effect of nanocrystals, which might not be visible in the early stages in a XRD diffraction pattern. The $Co_{44}Fe_{24}Y_5B_{27}$ melt spun sample imaged in Figure 4-5 was annealed at different temperatures ranging from 575°C to 615°C for 5 min in Ar atmosphere. While the XRD signal of the sample annealed at 580°C does not show any crystalline peaks (see Figure 4-5 a)), the crystallinity is already visible in the TEM diffraction pattern (see Figure 4-5 b)). The probed volume in a XRD experiment is much larger compared to a TEM diffraction experiment [99]. Because of this, the signal of a single nanocrystal might not be visible in the background of the XRD measurement. On the other hand, it can be difficult to find small features of interest in the small probed volume of the TEM samples. The two methods are used complementarily to avoid effects of crystallinity influencing the following more complex experiments. This is of great importance, because effects of partial crystallinity or nanocrystals are not a part of this work and their effects would be misleading for the interpretation of the results regarding the mechanical properties of the tested specimen.

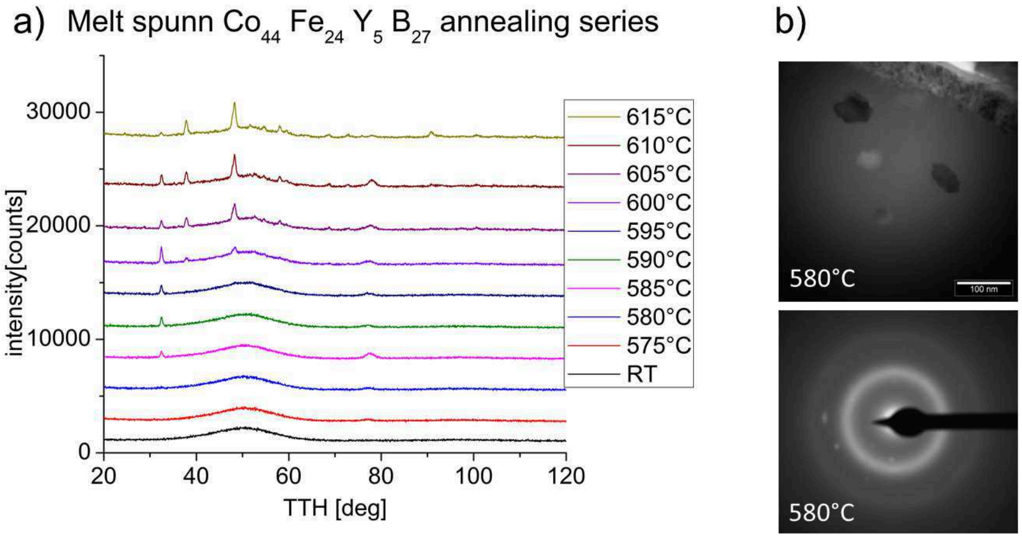

Figure 4-5: *Comparison of a $Co_{44}Fe_{24}Y_5B_{27}$ melt spun sample XRD annealing series a) which shows no crystallinity after a heat treatment to 580°C and TEM investigations b) (diffraction pattern and bright field image) containing nanocrystals after the same heat treatment.*

To prove the homogeneity of the investigated thin films, TEM bright field images are recorded. Figure 4-6 shows the examples of two Co-based metallic glasses. The thickness of the metallic glass layer is homogenous and contains no cracks. The Cr-adhesion layer of 64nm shows a sharp distinction and no considerable diffusion of Cr into the metallic glass took place.

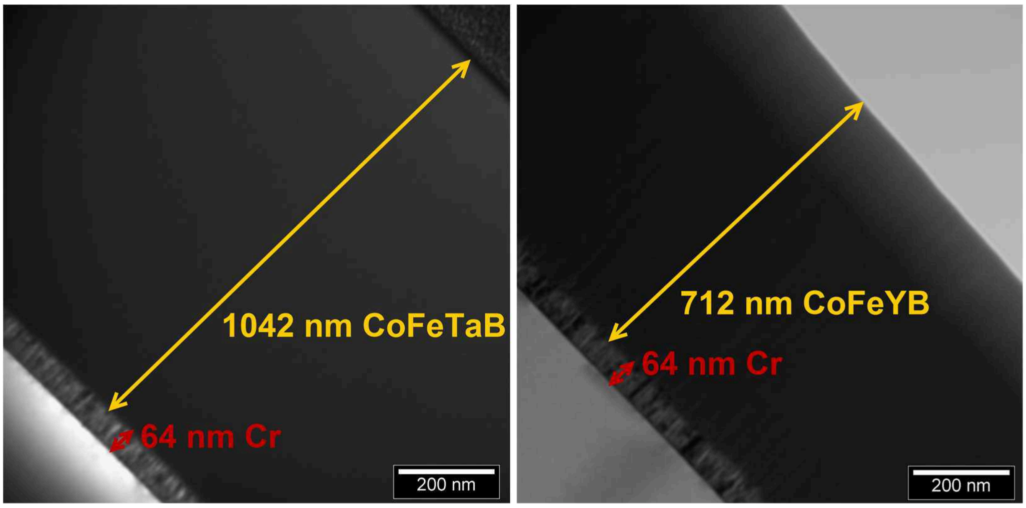

Figure 4-6: *TEM bright field images of $Co_{43}Fe_{22}Y_4B_{30}$ and $Co_{40}Fe_{19}Ta_7B_{34}$ thin films including the Si substrate (lower left) and the Cr adhesion layer.*

4.2.3 Differential scanning calorimetry (DSC)

By differential scanning calorimetry (DSC), it is possible to measure the amount of heat per time, which is necessary to increase the temperature of a certain amount of material. For quantitative analysis, a reference material of known heat capacity is simultaneously measured [100]. Melting is an endothermic process and, hence, additional heat is required to keep the temperature rise constant. The crystallisation of an amorphous material is an exothermic process. In order to keep the rate of temperature rise constant (10K/min) the heat induced by the DSC is reduced during the crystallisation process, which is visible in the recorded data (see Figure 4-7 T_c). Therefore, the DSC is an irreversible technique to test the amorphous state of a sample because once a sample is crystalline, it stays crystalline due to the limited cooling rates. Additional parameters, such as the glass transition temperature T_g, can be determined by this technique but are not in the scope of this work.

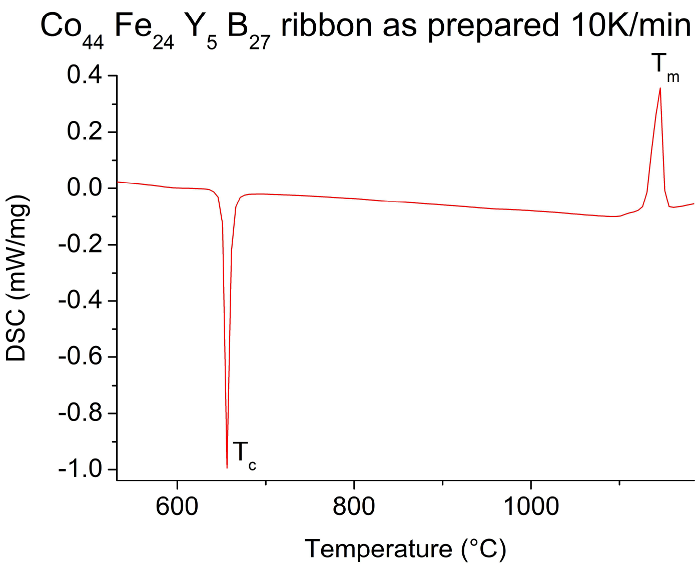

Figure 4-7: DSC curve of a melt spun $Co_{44}Fe_{24}Y_5B_{27}$ metallic glass sample showing the exothermic crystallisation peak T_c and the endothermic melting peak T_m.

4.2.4 Atom probe tomography (APT) as proof of chemical homogeneity

As discussed in section 3.5.3 the frequency distribution analysis of APT data sets can be a powerful tool to investigate the inner structure of analysed specimen. Figure 4-8 presents the frequency distribution for all metallic glass compositions, which have been tested by cantilever bending tests. The data sets were partitioned into bins of 100 atoms. The individual graphs show no relevant deviation (small χ^2) between the ideal binomial distribution (line) and the measured distribution (open circle) which indicates the homogeneity of the atomic distribution. All metallic glass compositions which were produced for mechanical testing reasons show no signs of nanostructure, such as segregation, clustering or preferential ordering.

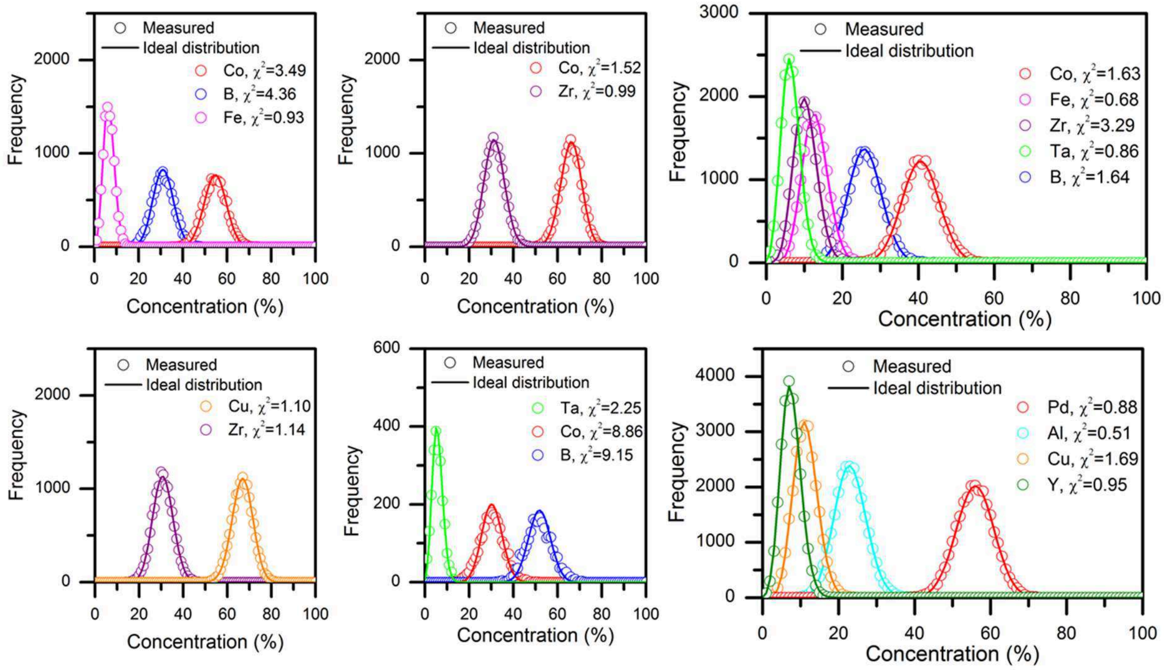

Figure 4-8: Frequency distribution analysis showing the homogeneity of all metallic glass compositions which have been investigated by bending experiments.

By applying the frequency distribution analysis, it is possible to exclude effects like the segregation of the material into amorphous nanoscale phases (shown in Figure 4-9). The χ^2 indicating the deviation between ideal and measured distributions is large and the heterogeneity of the specimen is indicated in the frequency distribution plots in Figure 4-9 c). The measured distribution is much broader than the ideal distribution and, therefore, the chemical composition of the sample is not distributed homogenously. The isoconcentration surfaces in Figure 4-9 a) show that the material segregates into two amorphous phases, namely Co-rich and Zr-rich. Furthermore, XRD patterns would characterise this material as amorphous because both phases are still amorphous [61].

The described example demonstrates the significance of using complementary techniques, such as XRD, TEM and APT, to fully characterise the as prepared condition of the produced metallic glass samples.

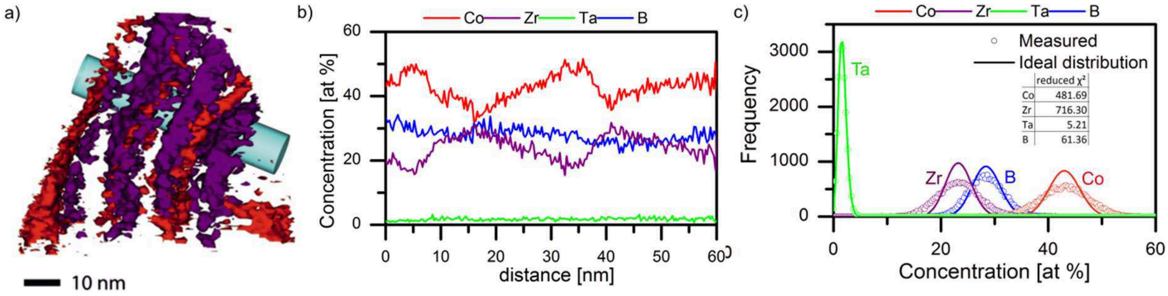

Figure 4-9: *a) APT reconstruction of a $Co_{44.7}B_{29.7}Zr_{23.9}Ta_{1.7}$ metallic glass sample showing the segregation (isoconcentration surface of 50.00 at% Co and 28.32 at% Zr) into amorphous Co and Zr-rich phases. The concentration profile b) is plotted along the cylinder in a) from left to right. The frequency distribution analysis in c) deviates from the ideal distribution [61].*

5. Experimental validation of models

The models applied within this work have been adopted from the literature [3, 36, 59, 64, 65, 101] and were not explicitly developed for the tasks discussed within this work. The validity and applicability of the models has to be considered and their limitations should be kept in mind. The materials chemistry department of the RWTH Aachen University performed and provided the MD simulation results.

5.1 Validation of *ab initio* MD simulation (elastic properties)

The elastic properties of the simulated metallic glass composition have been calculated at the RWTH Aachen University by applying the OpenMX code [37] after the relaxation of positions and volumes (stress free configuration, see 2.1.2) [97]. The Young's modulus *E* is calculated using the shear *G* and bulk *B* moduli [102]:

$$E = \frac{9BG}{3B + G} \qquad (30)$$

The Young's modulus (see 3.3) is easy to measure and hence a good reference for testing the simulated elastic property values. Different metallic glass samples have been investigated by nanoindentation to determine their Young's modulus. Figure 5-1 a) shows that the simulated and measured Young's moduli of a $Co_{43.5}Fe_{23.5}Y_xB_{33-x}$ melt spun and sputtered series are in good agreement. They only depend on the B/Y ratio. Being an intrinsic property, different production processes have no major influence on the Young's modulus. Instead, additional synchrotron diffraction experiments as described in the PhD thesis of Volker Schnabel [103] reveal the origin of the continuously raising E as an increase in the (Co,Fe)-B bond population due to the boost of B.

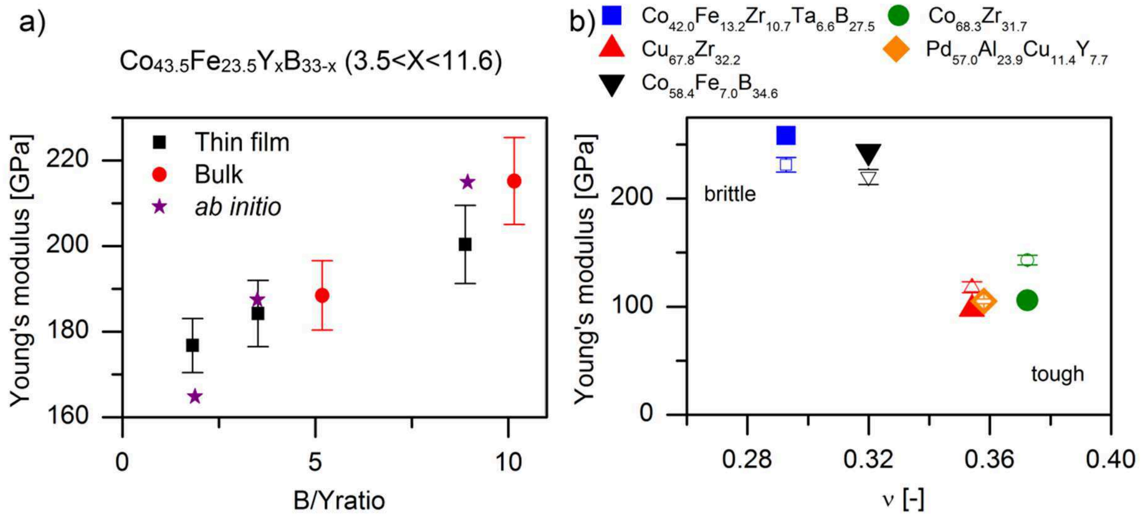

Figure 5-1: *Validation of ab initio MD simulations: a) By bulk and thin film synthesis of $Co_{43.5}Fe_{23.5}Y_xB_{33-x}$ (3.5<X<11.6) resulting in a B/Y ratio of 1.8 < B/Y < 10.2. b) By comparing experimental (open symbols + error bars) and simulated (filled symbols) results of various metallic glass thin films.*

The original approach by C. Hostert et al. [3] was approved for Co-based metallic glasses. The results in Figure 5-1 b) reveal the same good agreement between simulated and experimental data for non-Co-based metallic glasses, such as $Cu_{67.8}Zr_{32.2}$ and $Pd_{57.0}Al_{23.9}Cu_{11.4}Y_{7.7}$, which have been produced by sputter deposition. The investigated metallic glasses cover a wide range of the Poisson's ratio including the proposed brittle to tough transition around $\nu = 0.32$ [13].

The applied model delivers reasonable results and good agreement for all investigated specimen. Therefore, predictions of elastic properties for exclusively simulated compositions of metallic glasses are reliable.

5.2 Finite element method (FEM) simulation of fracture toughness (Abaqus)

The ratio of notch depth *a* and thickness *w* as well as the overall geometry of the cantilevers (see Figure 3-4) are of great importance for the validity of the proposed model. Matoy et al. [64] specify the region in which the function f(a/w) (equation (7)) is applicable as $0.05 < a/w < 0.45$. The dimensions of the cantilevers are supposed to be close to a ratio of $L{:}w{:}B = 5{:}2.1{:}1.7$. The fracture toughness of exemplary $Cu_{67.8}Zr_{32.2}$ cantilevers has been measured according to Matoy's model. In order to check for deviations due to different geometrical properties, the same cantilevers have been simulated using extended finite element analysis (XFEM) in Abaqus 10.1.

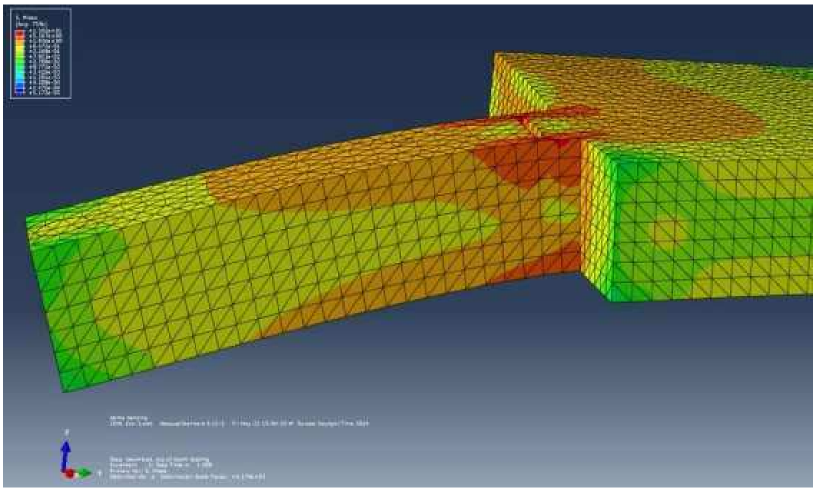

Figure 5-2: Example of the modelled cantilever including the mesh assigned showing the regions of high stress (red).

Each cantilever is individually modeled and simulated according to the procedure established by Jaya et al. [101]. The input parameters for simulating the mechanical properties were the Young's modulus of 114 GPa determined by nanoindentation and the Poisson's ratio calculated by MD simulations (1) as 0.354. A mesh is assigned to the modeled cantilevers to calculate and visualize the stresses and strains between the elements of the mesh (Figure 5-2). For the regions around the notch a more refined mesh is applied. The simulated cantilevers are loaded by a virtual indenter, according to the experimental loads.

The results are summarised in *Table 5-1* and show less than 5% deviation between the experimentally observed and simulated (XFEM) fracture toughness values. Matoy's model is also applicable for cantilevers, which show a slightly different geometry than the ones originally proposed.

L (µm)	w (µm)	B (µm)	F (µN)	a/w	K_{IC} (MPa*√m)	K_{IC} (MPa*√m) (XFEM)
6.513	2.657	2.876	370	0.339	1.40	1.46
6.157	2.684	3.313	605	0.335	1.83	1.85
7.761	2.864	3.477	460	0.314	1.44	1.52

Table 5-1: Comparison of K_{IC} calculated by analytical equation (6) from experimental results vs. XFEM (Abaqus) simulated values.

5.3 Dependence of notch depth on fracture toughness

The fracture toughness K_{IC} is determined by measuring the load-displacement curves of notched cantilevers and utilising equation (6). In order to estimate the effect of different *a/w* ratios on the fracture toughness, a systematic study has been carried out for the $Co_{42.0}Fe_{13.2}Zr_{10.7}Ta_{6.6}B_{27.5}$ composition.

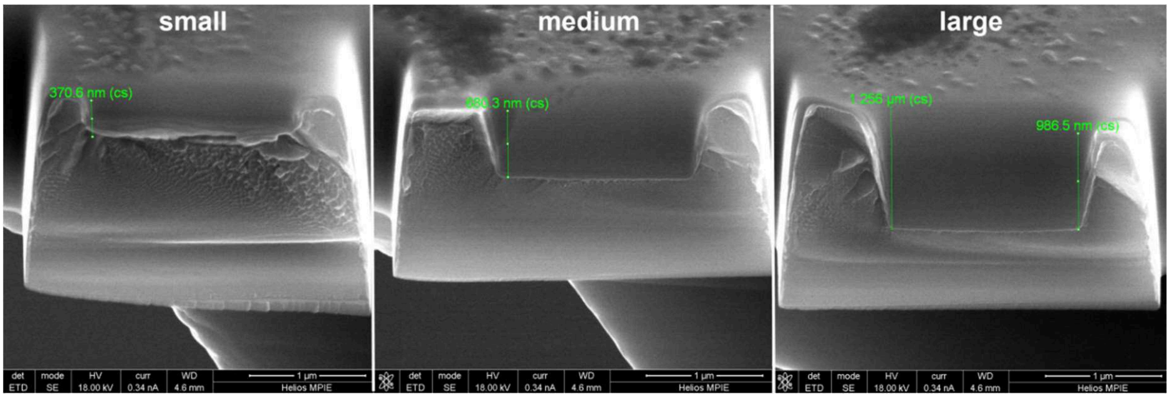

Figure 5-3: *Fracture surface SEM images of* $Co_{42.0}Fe_{13.2}Zr_{10.7}Ta_{6.6}B_{27.5}$ *metallic glass with increasing notch depth.*

A series of cantilevers with different notch depths have been prepared and measured according to 3.4.2. After the deformation process SEM images of the fracture surfaces showing the different notch depths are recorded (Figure 5-3). The strong effect of differing a/w ratios onto the fracture toughness is shown in Figure 5-4. It is obvious that the region where K_{IC} is independent of a/w is smaller than stated by Matoy et al. (see 5.2).

Complementing the observations made in 5.2 the a/w ratio is a much more critical quantity than the geometry of the cantilevers (*L,w,B*). Therefore, only cantilevers possessing an *a/w* ratio around 0.3 are considered in the following fracture toughness experiments.

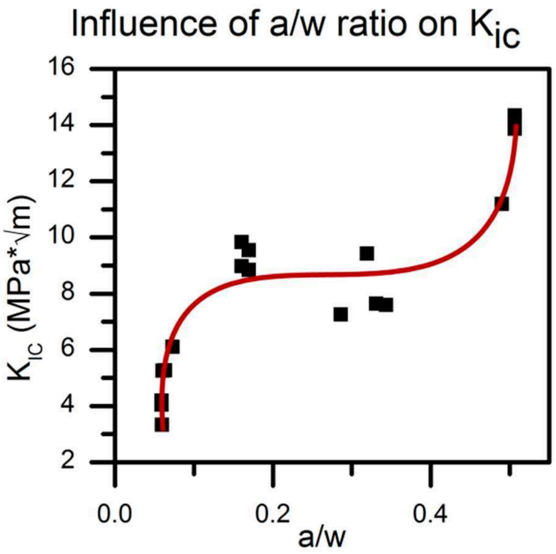

Figure 5-4: *K_{IC} in dependence of the a/w ratio for the $Co_{42.0}Fe_{13.2}Zr_{10.7}Ta_{6.6}B_{27.5}$ metallic glass showing the plateau where a/w does not affect the fracture toughness.*

6. Mechanical properties of metallic glasses in experiment

A main focus of this work is to gain a deeper understanding of the underlying chemical und structural mechanisms in metallic glasses which can lead to the development of new, ultra-strong metallic glasses. Therefore, it is necessary to gather reliable data on the mechanical properties of metallic glasses.

6.1 Bending tests

In 6.1.1 micro cantilever bending tests of metallic glass compositions covering a wide Poisson's ratio range were picked in order to cover the in 2.1.3 discussed brittle to tough transition (see Figure 2-6). The following compositions were suggested by the outcome of the MD simulations and produced by thin film sputtering:

Composition (at%)	Poisson's ratio ν
$Co_{68.3}Zr_{31.7}$	0.372
$Cu_{67.8}Zr_{32.2}$	0.354
$Co_{58.4}Fe_{7.0}B_{34.6}$	0.320
$Pd_{57.0}Al_{23.9}Cu_{11.4}Y_{7.7}$	0.358
$Co_{42.0}Fe_{13.2}Zr_{10.7}Ta_{6.6}B_{27.5}$	0.293

Table 6-1: Investigated compositions and their Poisson's ratio.

The precise compositions were determined by APT analysis and the Poisson's ratio was calculated using equation (1). G and B were calculated using the MD simulations, which have been refined after the compositions measured by APT. Lewandowski et al. [13] proposed criteria of Poisson's ratios describing the brittle to ductile transition in metallic glasses is disproved by calculating the fracture energy according to equation (11) and plotting the results into the Lewandowski graph (see Figure 2-6).

Additionally, in 6.1.2 a combinatorial CoTaB sample was investigated in order to analyse the influence of Co-B bonds. A Si wafer of two-inch diameter was coated as described in 3.2.1 and the composition was measured by EDX along 8 positions starting at the Co-rich side (see Figure 6-1). The distance between the positions was 4mm and in the centre (position 4) an APT sample was lifted out in order to calibrate the EDX spectrum. At each position 10 cantilevers were prepared (5 notched, 5 un-notched) as described in 3.4. By using the combinatorial approach a wide compositional range of $Co_{56.6}Ta_{9.9}B_{33.5}$ to $Co_{39.2}Ta_{5.8}B_{55.0}$ can be characterized.

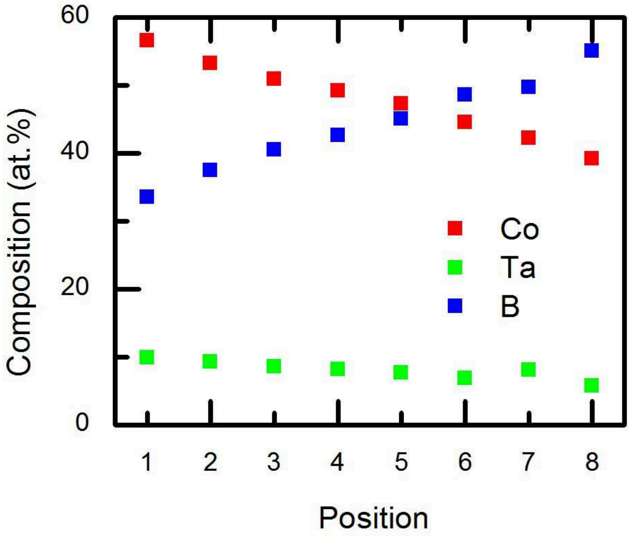

Figure 6-1: Compositional gradient along a combinatorial CoTaB thin film sample (positon distance 4mm) calibrated by an APT measurement in the centre.

6.1.1 Poisson's ratio and mechanical properties of metallic glass thin films

The metallic glass compositions shown in Table 6-1 were produced by thin film sputtering and their amorphous state and homogeneity have been proved by the methods discussed in section 4.2. Nanoindentation (Hysitron Inc., USA) was used to characterise the hardness and Young's modulus of the compositions as described in 3.3. Maximum loads of 4 µN were applied to stay within in the 10% film thickness limit for the indentation and the results were averaged over 100 indents. Notched and un-notched cantilevers have been prepared and tested according to section 3.4.

Bending tests

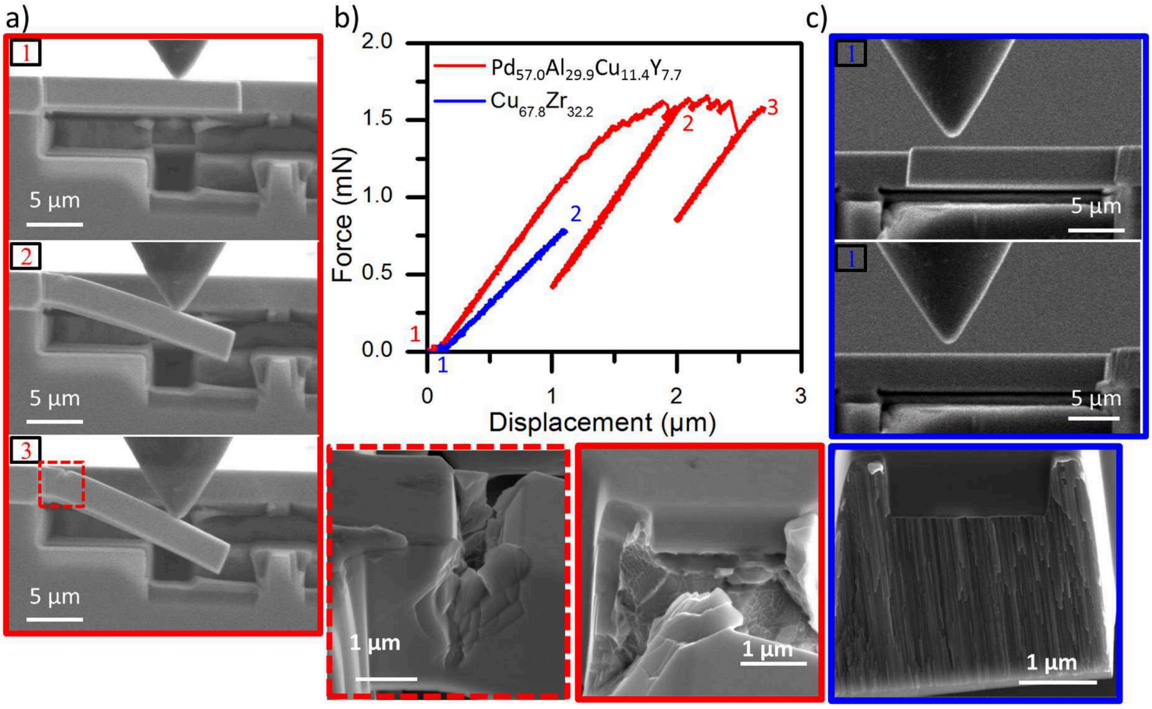

Figure 6-2: a) and c) SEM images of in situ cantilever bending test showing the deformation of the beam for a ductile / brittle metallic glass. The corresponding load-displacement curves are represented in b).

Figure 6-2 shows the characteristic sequence of events for two exemplary compositions. The ductile $Pd_{57.0}Al_{29.9}Cu_{11.4}Y_{7.7}$ sample (red) and the brittle $Cu_{67.8}Zr_{32.2}$ sample (blue) show different behaviour in the bending experiments. During the in-situ SEM observations the cantilevers are deformed constantly (displacement controlled). At some point the ductile beam is broken and no elastic tension counteracts against the indenter while it is retracted (Figure 6-2 a) image 1-3). The broken beam still sticks to the thin film and stays in the bent position. In contrast, the brittle beam is elastically loaded like a spring, flips out of the image and is gone at the moment of catastrophic fracture (Figure 6-2 c) image 1-2). The nature of fracture is also observable by the manner of the fracture surface.

In addition, the load-displacement curves in Figure 6-2 b) represent the mode of fracture: The brittle sample shows pure elastic deformation and abrupt catastrophic failure at the maximum load. In contrast, the load-displacement curve of the ductile sample indicates an immense amount of plastic deformation. The area underneath the load-displacement curves in Figure 6-2 b) represents the energy absorbed before fracture and this value is much larger for the ductile glass. Accordingly, the methods described in chapter 3.4.1 were applied to calculate the fracture toughness K_{IC} in the ductile (J-integral) and brittle case (linear elastics fracture mechanics). The fracture energy G_f has been calculated according to equation (11) using the K_{IC} values.

In a second series of bending tests, un-notched cantilevers have been deformed and fractured in the same way and the fracture strength σ is calculated according to equation (12) using the maximum load during bending.

Altogether, more than 100 cantilevers have been prepared and tested although 30% were “bad” tests due to oxidation effects or prohibited *a/w* ratios (see 5.3). Nevertheless, 12-16 valid bending experiments have been analysed per composition (50% notched, 50% un-notched) and their results are presented in Table 6-2.

	Composition (at%)	E (GPa)	ν	K_{IC} (MPa*√m)	G_f (J/m^2)	σ (MPa)
●	$Co_{68.3}Zr_{31.7}$	138	0.372	4.2 ±0.4	140	6240 ±410
▲	$Cu_{67.8}Zr_{32.2}$	114	0.354	2.7 ±0.1	60	3950 ±110
▼	$Co_{58.4}Fe_{7.0}B_{34.6}$	220	0.320	4.7 ± 0.2	100	7560 ±230
■	$Co_{42.0}Fe_{13.2}Zr_{10.7}Ta_{6.6}B_{27.5}$	231	0.293	8.0 ±0.4	280	8360 ±280
◆	$Pd_{57.0}Al_{23.9}Cu_{11.4}Y_{7.7}$	106	0.358	49.0	17400	4580

Table 6-2: Results of cantilever bending tests showing the simulated Poisson’s ratio ν and the Young’s modulus E from nanoindentation. The fracture toughness K_{IC}, fracture energy G and fracture strength σ were determined by micro cantilever bending tests.

The fracture energy G_f represents the energy that the material absorbs until the event of catastrophic fracture, and it indicates the damage tolerance of a material. The ductile $Pd_{57.0}Al_{29.9}Cu_{11.4}Y_{7.7}$ glass shows extensively higher fracture energy than the brittle Co-based ones. The mechanism of shear banding introduced by Spaepen [51] (see 2.1.3) is accountable for the dissipated energy during the elasto-plastic deformation of this Pd-based glass. It is conspicuous that the tough $Pd_{57.0}Al_{29.9}Cu_{11.4}Y_{7.7}$ glass and the brittle $Cu_{67.8}Zr_{32.2}$ show the same Poisson’s ratio of 0.35X, while their fracture energy deviates about three orders of magnitude. This is a strong indicator that the model proposed by Lewandowski et al. [13] is not sufficient: Poisson’s ratio is not a sufficient criterion to explain or predict the toughness or brittleness of glasses.

Bending tests

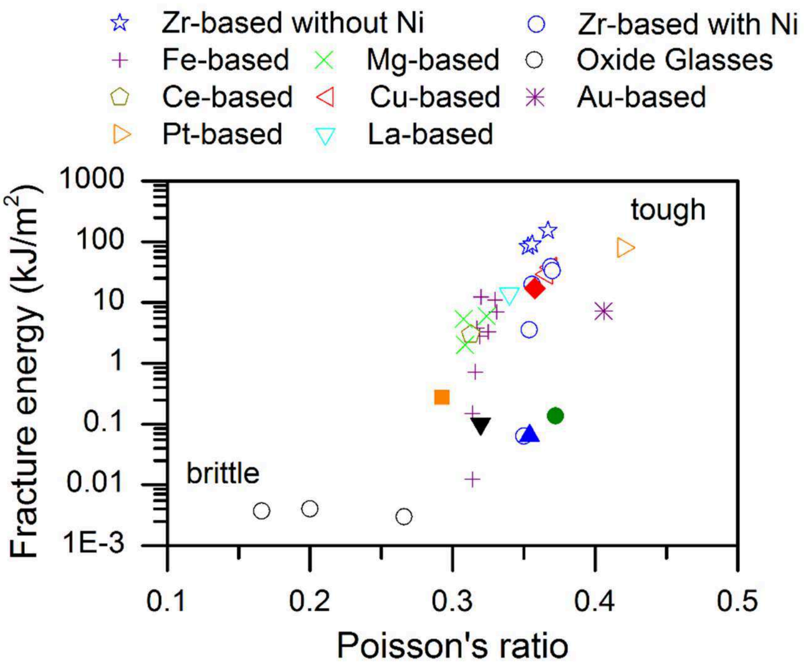

Figure 6-3: "Lewandowski plot" of data for the Mg-based, Ce-based and La-based [104, 105], Fe-based [4], oxide glasses [56, 106], Zr-based [107, 108], Cu-based [109, 110], Pt-based [111], Au-based [104] and Ge-Se chalcogenide glasses [112] from literature in comparison with data of this work (filled symbols) [14].

Figure 6-3 visualises the deviation of the proposed model by plotting the fracture energy in dependence of the Poisson's ratio. Additional literature data as well as the data of this work demonstrate that there is no sharp brittle to ductile transition in the proposed range of ν =0.32. Recent work done within the SPP-1594 by Nollmann et al. [54] support this statement. Minor alloying of $Pd_{40}Ni_{40}P_{20}$ with 1 at% Co or 0.6 at% Fe results in a tremendous change in mechanical properties, while the Poisson's ratio remains unaffected.

Instead, a new model based on the bonding nature of the alloying elements is proposed and developed in collaboration with the materials chemistry department of RWTH Aachen University [14]:

- A change in Poisson's ratio depends on a change in the bonding nature from covalent to metallic bonds.
- The proportion of bonds originated from deep core, hybridized states compared to the overall bonding characterizes the damage tolerance of metallic glasses.

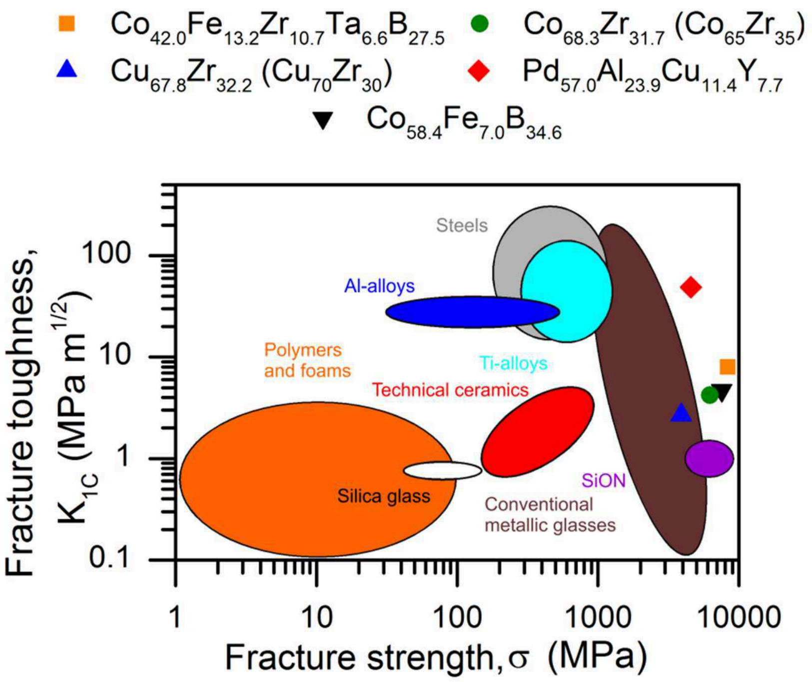

Figure 6-4: Fracture toughness in dependence of the fracture strength for different material classes from literature [64, 113, 114] including results of this work (single symbols) [14].

The fracture strength values of the metallic glass compositions investigated during this study are close to the theoretical limit of E/30. The region where traditional size effects become a major influence on the mechanical properties is reported to be in the range of below 100 nm for metallic glasses [115-117]. In comparison, the investigated samples are in the order of µm and no traditional size effect is expected. Instead, the exceptional high fracture strength values of this work are a result of the production method. The sputtering process enables to produce high quality, homogenous and almost defect free thin films. This is also supported by the fact that the measurements show very little scatter, which would not be the case for a material containing many defects.

The general approach of developing knowledge based alloying guidelines by systematic theoretical considerations and validating their outcome experimentally is a big improvement compared to the so far applied purely empirical approaches. Nevertheless, some limitations exist for predicting complex, macroscopic materials, because of the restricted dimensions (115 atoms) and the limited time scale (order of picoseconds) which are depicted by the MD simulations. Due to the mostly applied synthesis method, namely thin film sputtering, the samples show good homogeneity in terms of density and chemical composition. Additionally, the observed little scatter in the cantilever bending tests indicate only little occurrence of defects within the specimen. Therefore, the absence of macroscopic defects or cavities in the MD simulations has no major influence on the in 5.1 performed comparability of experiment and simulation. A fundamental property of metallic glasses is the glass forming ability, at least when it comes to the production of macroscopic sample sizes. The glass forming ability governs the necessary cooling rates, which have to apply in order to form an amorphous material. They depend on the mobility of the alloying elements as a function of the temperature and the thermal conductivity of the glass. Due to the limited time scale of the MD simulations, several picoseconds, it is not possible to account for these mechanisms, which operate on the time scale of microseconds. Accordingly, the described alloying guidelines do not consider the glass forming ability of metallic glasses.

6.1.2 Mechanical properties of a combinatorial CoTaB metallic glass thin film

The hardness and reduced Young's modulus were determined by nanoindentation (see 3.3) for each position (25 indents/position) of the sputtered thin films (see 6.1). As shown in Figure 6-5 the reduced Young's modulus and hardness increase with the increasing boron content. The reduced Young's modulus is used because the Poisson's ratio varies along the B concentration and is unknown. For the high-B content position the reduced Young's modulus reaches a value of E_{red} =344 GPa. This exceeds the Young's modulus of the so far reported record of E =309 GPa for a $W_{46}R_{37}B_{17}$ metallic glass by Ohtsuki et al. [1].

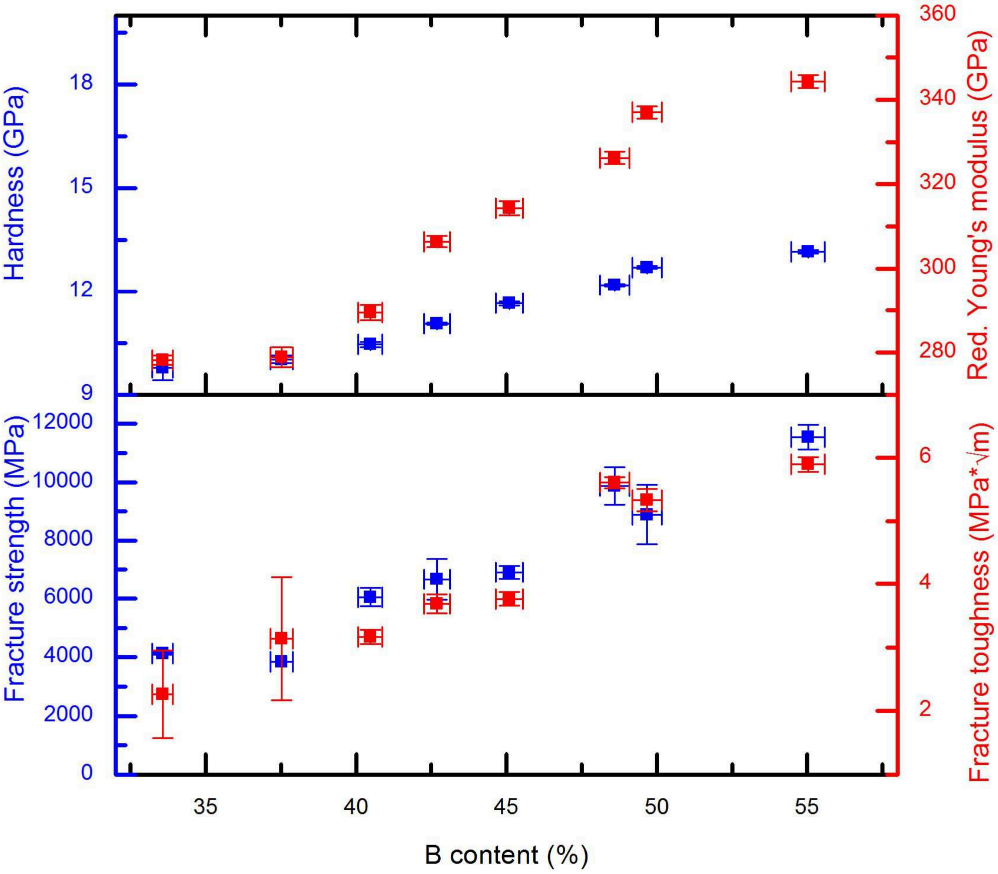

Figure 6-5: Top: Increasing trend of hardness and Young's modulus with increasing B content characterized by nanoindentation. Bottom: Increasing trend of fracture strength / toughness along the B gradient determined by micro cantilever bending tests. The y-error bars are derived from standard deviation, while the relative error in B content from EDX + APT reference is assumed to be 1% [118].

Bending tests

The trend of increasing mechanical properties with increasing B content applies also for the cantilever bending tests (see Figure 6-5 bottom). The fracture strength and fracture toughness increase with increasing B content. The fracture strength for the B rich position is in the range of σ =11 GPa which is more than twice the value of the reported record ultra-high strength $Co_{43}Fe_{20}Ta_{5.5}B_{31.5}$ bulk metallic glass with a fracture strength of σ =5185MPa by Inoue et al. [2]. A fracture toughness of 6 MPa√m is accomplished for the B rich composition.

The high values in Young's modulus can be explained by the same observations made in 5.1 and the synchrotron diffraction experiments (PDFs) carried out by Volker Schnabel in Figure 6-6. The observations are similar to the findings of Schnabel et al. [61, 119] where a boost of B content emerges into an increase of metal-B-bonds and therefore raising Young's modulus. The increase of Co-B-bonds with increasing B content is represented in Figure 6-6 by the area of the first peak at 2.0 Å. For more detailed information on the performed synchrotron experiments and the consistent *ab initio* studies I recommend the PhD thesis of Volker Schnabel [103].

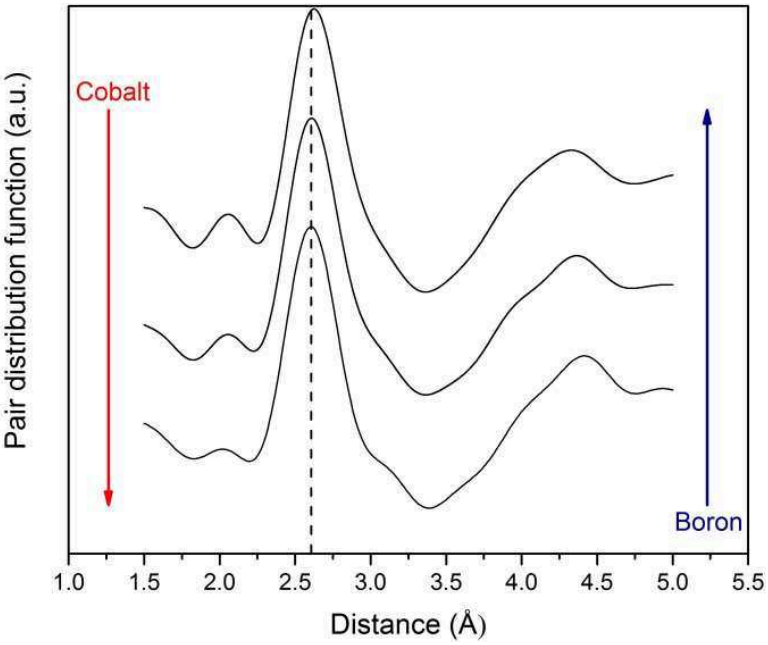

Figure 6-6: The experimentally obtained pair distribution functions with increasing B content from bottom to top. The area of the peak at 2.0 Å represents the amount of Co-B-bonds and increases with increasing B content.

Figure 6-7 summarizes the investigations of the structural and chemical compositions by TEM (Yen-Ting Chen, RWTH Aachen University) and APT, which reveals a structural evolution within the combinatorial sample. While the low B sample contains a homogenous, single-phase material without clusters or lamellas, this changes with increasing B content. The medium B content sample shows decomposition into a B rich $Co_{49.4}Ta_{9.6}B_{41.0}$ and a B depleted $Co_{61.8}Ta_{10.9}B_{27.3}$ phase. The phases form in a lamellar structure with a spacing of ≈25 nm. The high B content sample decomposes into a B rich $Co_{35.0}Ta_{12.2}B_{52.8}$ and a depleted $Co_{40.6}Ta_{12.6}B_{46.8}$ phase. Here the lamellar structure is much more refined on a length scale <5 nm. Synchrotron diffraction patterns proved the amorphous character of all observed phases.

As described in 2.1.3, the formation of shear transformation zones (STZs) results in the nucleation of shear bands, which are the responsible deformation mechanism in metallic glasses. The hypothesis for the in Figure 6-5 observed high fracture toughness/strength values with increasing B content is, that the formation of STZs and shear bands is suppressed by geometric constrains due to the lamellar structure. Pan et al. [46] report the experimental size of STZs is in the range of several nm^3. According to Shimizu et al. [48], the formation of a group of STZs which form at defects and impurities is necessary to serve as the nuclei of a shear band. These shear bands develop and propagate after they have reached a critical length of ≈100 nm.

The fine lamellas observed in Figure 6-7 for the B rich sample are in the same order of magnitude as the STZs. The mechanism of STZs grouping together is somehow suppressed by the presence of a fine lamellar structure <5 nm and therefore the formation of a shear bands is more difficult and higher external stresses are necessary for a macroscopic deformation. It is well known, that dislocations in crystalline materials, which are line defects, are mobile, and as consequence can migrate and therefore accumulate within the material. In contrast, STZs in amorphous materials are point defect like defects with dimensions in the range of <6 nm^3 which are essentially immobile [45]. If the different compositions in Figure 6-5 experience external loading from the cantilever bending experiments, STZs form in the material. In the high B content, fine lamellar case, these STZs might only form in the mechanically weaker of the two phases. Within the small lamella dimensions of less than 5 nm it is not possible to accumulate enough STZs to nucleate a shear band. Only after the stresses are high enough, and STZs also form in the second, tougher phase, a necessary group of STZs is present and a shear band can nucleate.

For the medium B content case with lamellar spacing of around 25 nm a slightly different mechanism might be responsible for the increased fracture toughness/hardness. In the 25 nm-sized lamellas, enough STZs can accumulate and serve as nuclei for shear bands. The shear bands have to exceed a critical length of ≈100 nm in order to propagate and develop into a mature shear band. Eventually this leads to similar picture but on a larger length scale: shear bands form in the mechanically weaker of the two phases but they do not exceed the critical length until the external stresses increase further and shear bands also form in the tougher phase.

A systematic study of nanolaminated metallic glasses, produced by sputtering different thicknesses of layers in the dimensions of STZs and slightly different chemical compositions, as suggested by V. Schnabel [103], might help to further investigate and explain the current results. Another approach to gain a deeper understanding of the discussed mechanisms might be to investigate samples of varying deformation state, from undeformed to catastrophic failure, by correlative APT/TEM experiments in order to investigate the evolution of shear bands depending on the stress condition.

In general, the effect of suppressing the nucleation of shear bands by geometric constraints can be used as one of the design criteria for metallic glasses.

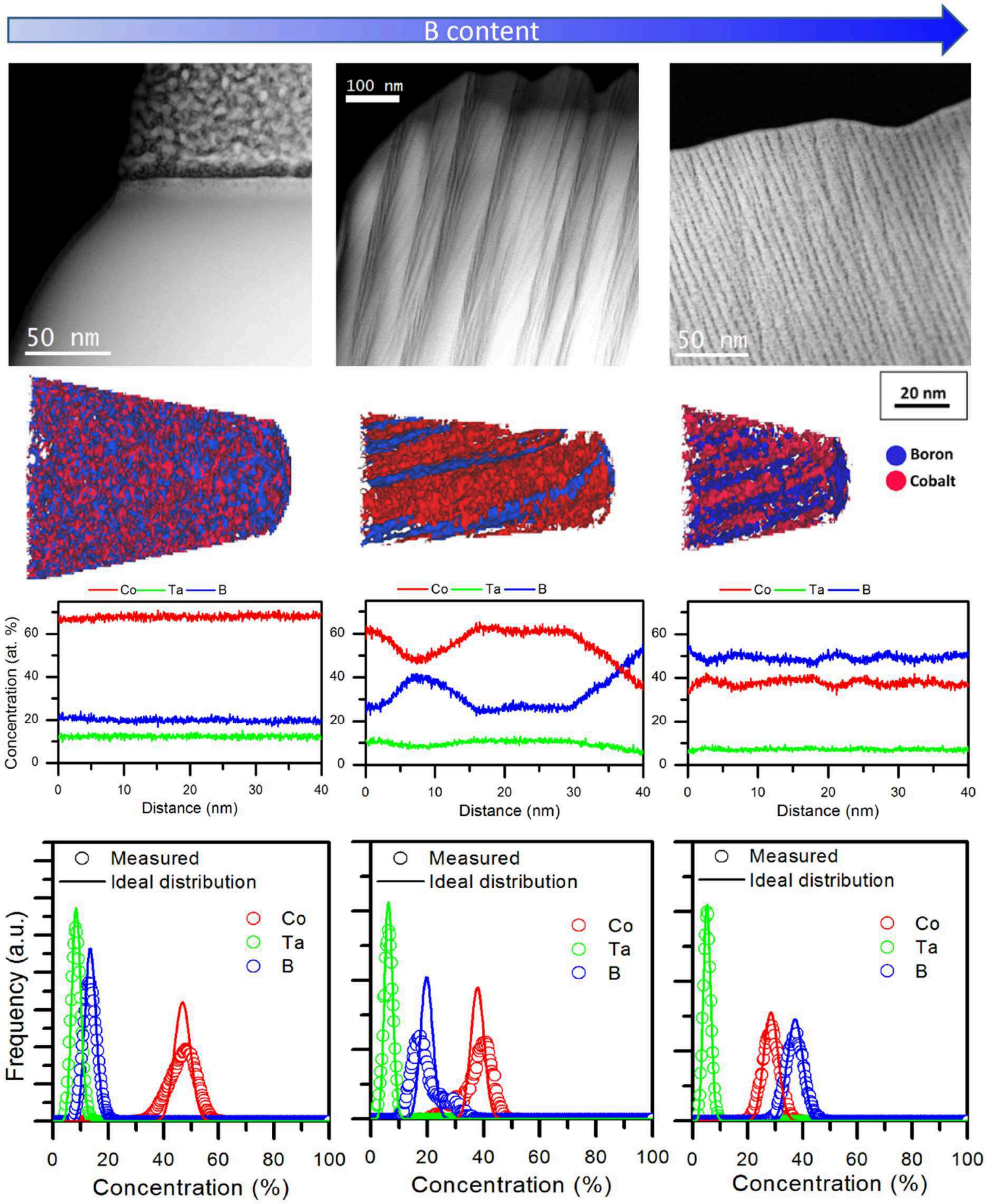

Figure 6-7: *Structural evolution in dependence of the B content. TEM images by Yen-Ting Chen, RWTH Aachen University show the transition from a homogenous 1-phase material towards a fine lamellar structured one. The APT images reveal the chemical composition of the formed amorphous phases.*

6.2 Shear banding in amorphous materials

The mechanism of shear banding in metallic glasses as characterised in section 2.1.3 is well established and described in the literature [42, 45, 51, 120, 121], although, the underlying physical and chemical relationships are not fully understood.

The thickness of shear bands is generally determined by TEM studies and a thickness of 10-20 nm [47, 122] is well-established and accepted. The potential temperature rise within shear bands and their inner amorphous / nanocrystalline / crystalline structure, the compositional changes as well as the existence of free volume in shear bands, are subject to controversial discussions [123-126].

One aspect of this work is to perform APT analysis on deformed metallic glasses in order to identify possible chemical gradients in shear bands, which will lead to a better understanding of the deformation mechanism in amorphous materials. These experiments are carried out in a correlative TEM/APT approach as described in 3.7 and, therefore, it is possible to link density changes observed by HAADF-STEM to chemical changes observed by APT.

6.2.1 TEM investigations of heavily deformed $Al_{88}Y_7Fe_5$ metallic glass

Our colleagues in the SPP-1594 from the materials department of Münster University who developed a method to measure the densities of shear bands (see 3.6.3) focused on the $Al_{88}Y_7Fe_5$ metallic glass due to the good contrast conditions for shear bands it shows in HAADF-STEM mode.

They produced a melt-spun ribbon of $Al_{88}Y_7Fe_5$ and a high shear band density was achieved by cold rolling the material. TEM lamellas were prepared at the MPIE by FIB milling according to 3.6.4 and investigated by the colleagues in Münster on a FEI Titan 80-300 TEM at 300kV in HAADF-STEM mode [5]. The chemical composition is determined by EDX and represented in Table 6-3.

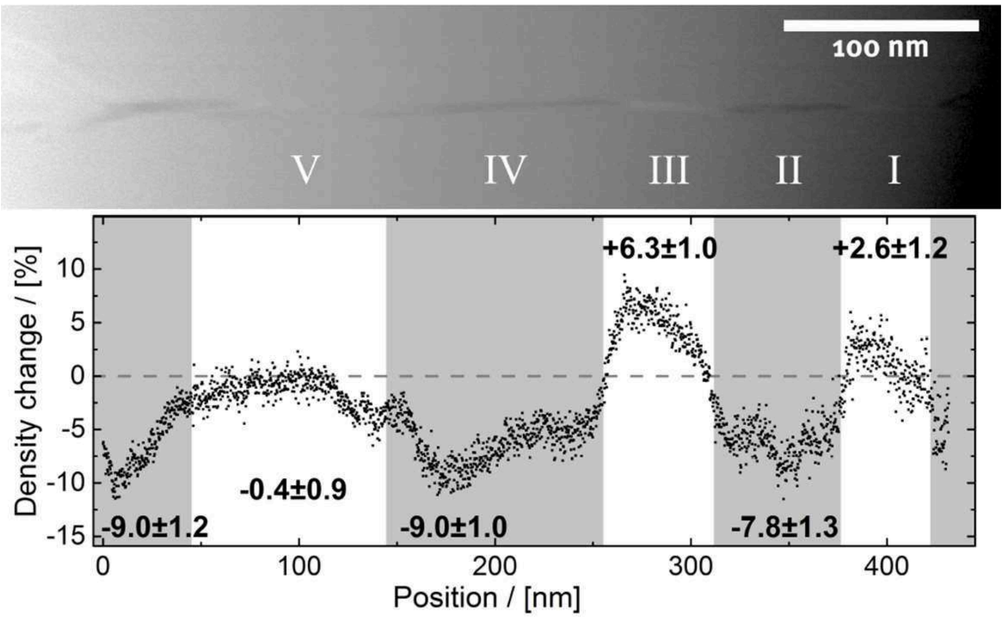

Figure 6-8: Density along the propagation of a shear band [5] by HAADF-STEM. The bright and dark parts indicate regions with higher (bright) and lower density (dark). On the right end of the shear band a bifurcation is observable.

As reported by Rösner et al. [92] the shear band shown in Figure 6-8 changes its contrast alternately from bright to dark which indicates its density change according to equation (29). The observed density changes range from -9.0 ±1.0% to +6.3 ±1.0%. The matrix shows no density fluctuations and seems to be unaffected. Additionally, the change in contrast/density is accompanied by a small deflection of the shear band (±5°) along the propagation direction. The thickness of the measured shear band is about 6 nm in width.

Their energy dispersive X-ray spectroscopy (EDX) data suggests a compositional change of the different parts of the shear bands as visualized in Table 6-3. The combination of density measurements and EDX data lead them to the conclusion that the density change is almost completely related to the change in chemical composition within the shear bands. Literature reports a phase separation on the nanoscale during crystallisation for the $Al_{88}Y_7Fe_5$ metallic glass [127]. Therefore, Rösner et al. used nanobeam diffraction patterns (NBDP) and fluctuation electron microscopy in order to investigate the amorphous/crystalline nature of the observed shear bands. They concluded that the dark parts of the shear bands show a mixture of an amorphous/crystalline structure or medium range ordered domains [5, 92].

Element (at%)	Shear band (dark)	Shear band (bright)	Matrix
Al	89 ±1.5	86.3 ±1.9	88 ±0.6
Fe	3.7 ±0.5	6.3 ±0.8	4.9 ±0.2
Y	6.9 ±1.3	6.9 ±1.7	6.7 ±0.5
Ga	0.4 ±0.3	0.5 ±0.4	0.4 ±0.1

Table 6-3: Chemical composition of shear bands as observed by Rösner et al. [5] compared to the matrix using EDX.

6.2.2 APT investigations of deformed $Al_{88}Y_7Fe_5$ metallic glass cantilevers

Because the chemical characterisation of shear bands by EDX has some uncertainties on the observed small length scale we applied APT measurements in order to investigate the assumed compositional changes within shear bands with high chemical and spatial resolution. To clearly identify shear bands in the reconstructed APT tips, the in 3.7 described correlative TEM/APT approach is chosen.

The APT specimens are prepared from the heavily deformed regions of the deformed cantilevers according to 3.7.1. It is important to keep the time periods between single experiments (FIB, TEM, APT) as short as possible to prevent the formation of oxide caps on the tips. The formation of oxide caps can be reinforced by electric fields due to electrostatic charging during the transport [128]. Special care was taken and we maintained constant grounding during the lifetime of a specimen from the moment of lift out until the APT experiment in order to minimize oxide formation. If oxide caps form, the yield of APT experiments drops dramatically due to the differences in the intensity of field evaporation for the specimen and the oxide cap. Therefore, an additional cleaning step is inserted in form of low kV FIB showering.

The complex and prone to fail series of performed actions and experiments is as follows:

1. Synthesis of thin films by the materials chemistry department at RWTH Aachen University according to 3.2.1.
2. Preparation of cantilevers by FIB according to 3.4.2.
3. Deformation of cantilevers by *in situ* SEM according to 3.4.3.
4. Sample preparation of APT/TEM specimens for correlative measurements by FIB according to 3.7.1.

5. Imaging of the specimens in the JEOL 2200FS TEM in HAADF-STEM mode to identify shear bands.
6. Cleaning of the specimens by low kV FIB showering or, if necessary, shortening of tips by FIB and repetition of step 5.
7. Measurement of specimens in LEAP 3000X HR APT in voltage mode at 200kHz pulse rate, 20% pulse fraction, 50K and 0.5% target evaporation.
8. If specimens are not fractured in step 7, imaging of measured tips in the JEOL 2200FS TEM in HAADF-STEM mode to improve the dimensions of the APT reconstruction.

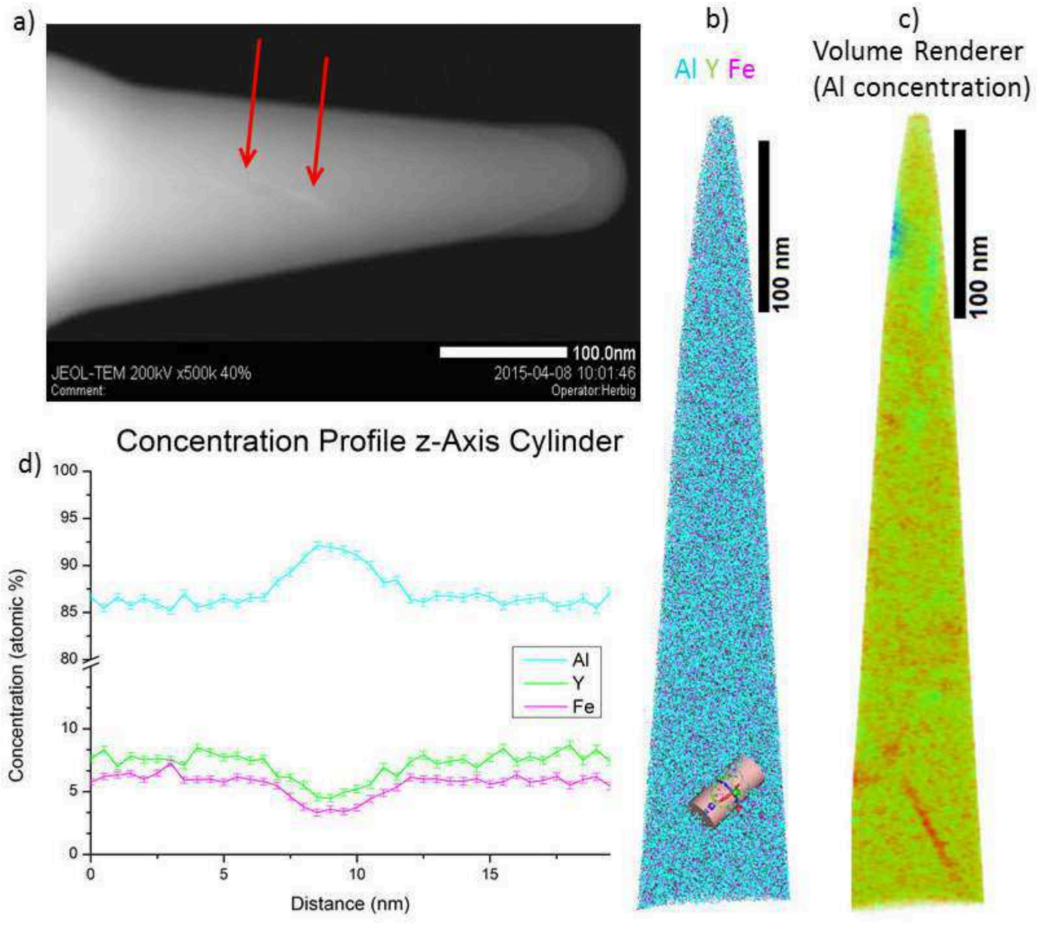

Figure 6-9: *Correlative APT/TEM investigations of heavily deformed $Al_{88}Y_7Fe_5$ metallic glass. a) shows the HAADF-STEM image of an APT tip including the bright and dark part of shear band indicated by re arrows. b) shows the reconstructed APT tip and indicates the position where the in d) plotted concentration profile is taken. c) displays the Al concentration along the reconstructed tip and the position of the shear band is clearly visible as region with increased Al concentration.*

Shear banding in amorphous materials

Figure 6-9 a) shows the HAADF-STEM image of an $Al_{88}Y_7Fe_5$ metallic glass tip which contains a shear band indicated by the red arrows. The images are taken at a camera length of 4 cm because systematic studies on the camera length of Schmidt et al. [92] reveal that short a camera lengths improve the normalized intensity signal. The shear band consists out of the characteristic dark and white parts as discussed in 6.2.1 and is located within the first 200 nm of the tip. At the top of the specimen the oxide cap is visible which illustrates the importance of the cleaning step 6.

After the successful APT run of 30.7 million collected atoms, using the parameters described in step 7, the dataset is reconstructed using IVAS 3.6.8 voltage reconstruction. In Figure 6-9 c) the position of the shear band is clearly visible as a region with increased Al concentration. By the volume renderer, a tool implemented in IVAS which simply visualizes the concentration gradients within a sample using a temperature colour map [76], the easy positioning of the region of interest cylinder as shown in b) is possible. In d) the concentration profile along the z-axis of the cylinder, which is placed perpendicular to the shear band is plotted.

By fitting a Gaussian profile to the observed concentration profiles, the thickness of the investigated shear band is determined to be in the range of ≈9 nm. This corresponds with literature values [47, 122] as well as the observations made by Rösner et al. [5] on the exact same material. Inside the shear band the concentration profiles reveal an increase of Al content to 92.2 ±0.3%, while Y and Fe are depleted to 4.5 ±0.2% and 3.3 ±0.2% respectively. It is important to notice that the matrix seems to be unaffected and shows no depletion of Al or enrichment of Y and Fe. The individual concentrations as well as the molar masses *M* and atomic numbers *Z* of the different regions and their relative changes are summarized in Table 6-4. The absolute and relative molar volumes *V* are calculated including the HAADF-STEM data of section 6.2.1 and are therefore marked with *.

	Shear band	Matrix
Al (at%)	92.2 ±0.3	86.2 ±0.1
Fe (at%)	3.3. ±0.2	6.1 ±0.1
Y (at%)	4.5 ±0.2	7.7 ±0.1
M (g/mol)	30.3 ±0.2	33.0 ±0.2
$\Delta M = (M_{SB}-M_M)/M_M$ (%)	-8.11	
Z	14.48 ±0.08	15.64 ±0.08
$\Delta Z = (Z_{SB}-Z_M)/Z_M$ (%)	-7.43	
V* (cm^3/mol)	9.81 ±0.08	9.96 ±0.08
$\Delta V^* = (V_{SB}-V_M)/V_M$ (%)	-1.56	

*Table 6-4: Chemical compositions of shear band and matrix as observed from the concentration profile by APT reconstruction. Absolut and relative molar masses M, ΔM and atomic numbers Z, ΔZ are calculated from the individual concentrations. The absolute and relative molar volumes V, ΔV are calculated using the absolute density values of the HAADF-STEM investigations [5] and therefore are marked with a * because they are not exclusively APT results.*

By HAADF-STEM (see Table 6-3) an increase of Al for the dark part of a shear band is observed and the APT data (see Table 6-4) shows the same trend. As discussed in 3.6.3, the HAADF-STEM signal is proportional to Z^2. Therefore, regions with high *Z* appear bright in HAADF-STEM mode and vice versa. The relative change in atomic number *ΔZ* between the shear band and the matrix as observed in the APT reconstruction is -7.43% which means that a dark segment of a shear band was investigated. One of the reasons why the analysed APT dataset only contains a dark segment of a shear band, while the HAADF-STEM image of the tip clearly shows a dark and a bright region, might be the limited field of view during the APT experiment. During an APT run not the complete specimen volume is projected onto the detector, depending on the shape and material of the tip and the overall geometrical setup, such as flight length and detector size [72]. Another reason might be that the APT specimen fractured right before the bright part of the shear band was about to be analysed as it can be seen that the shear band in Figure 6-9 c) propagates to the bottom right of the analysed volume.

Relative densities of the shear bands analysed by the HAADF-STEM method in 6.2.1 can be converted into absolute values, by using the absolute value of the $Al_{88}Y_7Fe_5$ matrix which has been evaluated as part of a diploma thesis done at Münster University. Using the absolute values of the molar mass *M* and density *ρ*, the molar volume *V* of shear band and matrix can be calculated according to $V = M/\rho$. The relative change of molar mass between shear band and matrix is ΔM =-8.11%, while the relative change of molar volume is only ΔV =-1.56%. Hence it can be concluded that the majority of the observed density change in 6.2.1 is related to compositional changes, while the volume stays rather constant.

The fact that the matrix of the investigated $Al_{88}Y_7Fe_5$ metallic glass seems to be completely unaffected by the compositional changes within the shear bands raises some questions. The matrix shows no indication of chemical depletion or enrichment of any kind as observed by APT investigations (see Figure 6-9). Off course fundamental rules like the conservation of mass have to apply and the overall composition of elements has to be constant. This indicates that the observed compositional changes of the bright and dark regions of a shear band compensate each other. The origin and driving force for the transport of material exclusively within the shear bands on length scales of several 100 nm is still unknown.

Reports in literature on temperature rise during shear band formation [129-131] as well as their propagation speed [132-134] are contradictory and vary by several orders of magnitude. The formation of crystals or “order” within shear bands is also widely discussed and not universally proved or disproved [135-138]. Due to the nature of shear bands it is extremely challenging, if not impossible, to perform experimental *in situ* observations during the formation of a single shear band. One option to gain a better understanding of the deformation mechanism in metallic glasses might be to apply computer simulations using the gathered information regarding density, composition and volume change as planned within the SPP-1594. From the increase in diffusivity, which is necessary in order to achieve the obtained material transport within shear bands, the propagation speed and temperature could be estimated.

7. Summary

The objective of this work was to evolve new, knowledge based alloying guidelines for ultra-strong metallic glasses and the development of metallic glasses which exhibit exceptional mechanical properties. Additionally, the basic deformation mechanisms of metallic glasses were in the interest of this work, especially an improved understanding of shear banding was desired. Therefore, a variety of Co-based and non-Co-based metallic glasses were synthesized based on theoretical considerations derived from MD simulations using melt spinning (m) or magnetron sputtering (s):

- $Co_{68.3}Zr_{31.7}$ (s)
- $Cu_{67.8}Zr_{32.2}$ (s)
- $Co_{58.4}Fe_{7.0}B_{34.6}$ (s)
- $Pd_{57.0}Al_{23.9}Cu_{11.4}Y_{7.7}$ (s)
- $Co_{42.0}Fe_{13.2}Zr_{10.7}Ta_{6.6}B_{27.5}$ (s)
- $Co_{43.5}Fe_{23.5}Y_XB_{33-X}$ ($3.5<X<11.6$, 5 steps) (s,m)
- Combinatorial $Co_{56.6}Ta_{9.9}B_{33.5}$ to $Co_{39.2}Ta_{5.8}B_{55.0}$ (s)

Their amorphous character of the as prepared state was proved for all compositions by XRD, TEM, APT and DSC in order to exclude contributions of partial crystallisation or other effects on the mechanical properties. The combinatorial CoTaB thin film metallic glass in 6.1.2 showed decomposition into two lamellar amorphous phases, while all other investigated compositions were chemically homogenous.

The applied models for the micro cantilever bending tests and MD simulations were validated. The limits and applicability of the analytical formulas for the fracture experiments were tested by FEM simulations, which show less than 5% deviation. Hostert et al. demonstrated the potential of MD simulations for predictions of elastic properties for Co-based metallic glasses [3]. Experimental data of this thesis in comparison with simulations done by Schnabel [103] reveal the universal integrity of this concept.

Mechanical properties of the individual compositions were determined by nanoindentation and cantilever bending tests. Exceptional high values of reduced Young's modulus E_{red} =344 GPa and fracture strength σ =11 GPa are reported for the B rich composition of the combinatorial CoTaB sample, exceeding the so far reported world record metallic glasses [1, 2]. A combination of changing micro structure and an evolution of the bonding types with increasing B content are the reasons for the observed high stiffness and toughness. The structure evolves from a homogenous one phase material towards lamella shaped two phase material and, therefore, suppresses the nucleation of shear bands. With increasing B content more Co-B bonds are present and the stiffness is increased.

A series of five metallic glass compositions with varying Poisson's ratio ν =0.293 to ν =0.372 were tested. The by Lewandowski et al. [139] proposed relationship between Poisson's ratio and toughness of metallic glasses with a sharp transition from brittle to ductile at ν =0.32 was not observed. Instead, a new model based on the bonding nature and the electronic structure of the alloying elements is proposed and developed in collaboration with the Materials Chemistry department of the RWTH Aachen University [14]:

- A change in Poisson's ratio depends on a change in the bonding nature from covalent to metallic bonds.
- The proportion of bonds, originated from deep core, hybridized states compared to the overall bonding, characterize the damage tolerance of metallic glasses.

Shear banding is the responsible deformation mechanism in metallic glasses and their nature was studied in more detail for an amorphous $Al_{88}Y_7Fe_5$ system. TEM investigations in collaborations with the materials physics department of Münster University revealed relative density changes of -9.0 ±1.0% to +6.3 ±1.0% compared to the matrix [5]. The compositional changes of shear band and matrix were investigated by correlative TEM/APT. For a dark segment of a shear band, relative changes in composition of +7.0 ±0.5 at% for Al, -46 ±5 at% for Fe and -42 ±5 at% for Y compared to the matrix were detected. A comparison of relative molar volume change and relative molar mass change demonstrates that the mass transport is the dominant mechanism affecting the density variations. The absence of density changes and the non-existence of chemical fluctuations in the matrix lead to the conclusion that material transport is only happening within shear bands, while the matrix is unaffected.

8. Outlook

The scope of this work was subject to some restrictions due to the limitations given by SPP-1594 which was established to “generate the knowledge that is necessary for developing glasses with superior mechanical properties” [140]. Every now and then, interesting and promising aspects, like corrosion resistance or effects of systematic heat treatment of metallic glasses, opened up but could not be investigated in detail.

Nevertheless, explicitly the corrosion resistance properties of metallic glasses, show a lot of potential and are worth investigating as several publications demonstrate [141-143]. During this thesis melt spun CoFeYB ribbons (see 5.1) were synthesized and it was not possible to manufacture them into TEM sample discs by electro polishing [144], because no suitable etching solution could be found. As reported in the literature [7], the corrosion resistance in metallic glasses benefits from the lack of fast diffusion pathways, such as grain boundaries and dislocations. Thus, systematic electrochemical corrosion experiments would be of great interest. Especially, in combination with the already existing data of MD simulations and bond characteristics this might be an interesting field of research.

Another proposed idea is to further investigate the deformation mechanism of metallic glasses, in particular the formation of shear bands by correlative APT/TEM. Additional investigations of different classes of metallic glasses have to be performed, because it is not clear whether the in $Al_{88}Y_7Fe_5$ observed compositional changes between matrix and shear band are universal for metallic glasses. The work on the formation of shear bands by Shimizu et al. [48], discussed in 6.1.2, is of purely theoretical nature and experimental proof is extremely challenging but possible. The postulated existence of embryonic shear bands, which have to grow up to a critical length of ≈100 nm until they can propagate, could be tested by investigating a series of continuously deformed samples. Due to the difficulties of getting reasonable contrast in the HAADF-STEM signal (see 6.2.1), a wise material selection has to be considered in order to image subcritical shear bands. *In situ* TEM deformation experiments in HAADF-STEM mode might also help to provide some clarity. Potentially, these kinds of investigations could also be extended to oxide glasses. The also in 6.1.2 described relationship between STZs and shear bands is unlikely to be proved experimentally, due to the nature of STZs. A combined approach of feeding as much experimentally accessible data into computer simulations might improve the understanding of STZs further.

Finally, it is planned to characterize mechanical properties of bulk metallic glasses (BMGs) with dimensions above 1 mm in thickness. These kind of dimensions can be achieved by mold casting [145]. Our collaboration partners at the materials department of Münster University are experienced in mold casting metallic glasses and agreed on providing us with samples of CuZrAlNb glass. It is proposed that these samples are shaped into standard tensile test geometry [146] and tested according to the well-established test methods. For comparison, a material with the same composition is synthesized by thin film sputtering and their mechanical properties are tested according to the methods utilized in this thesis (see 3.4). Correlating the mechanical property data of both methods should give strong support for the acceptance of the micro cantilever bending test method and the application of thin film sputtering. Controversial discussions with reviewers of the metallic glass community on the validity of cantilever bending tests and their comparability to standard BMG tensile tests should fade after successful experiments. The approach will also help to establish the method of thin film sputtering with all its advantages, such as good chemical and structural homogeneity or the possibility of combinatorial sample preparation, further because a reliable and well-established test method for mechanical properties of thin films is available. Preparing and characterizing BMGs might also be a step towards more application-related materials.

9. References

1. Ohtsuki, M., et al., *Hard metallic glass of tungsten-based alloy.* Applied Physics Letters, 2004. 84(24): p. 4911.
2. Inoue, A., et al., *Ultra-high strength above 5000 MPa and soft magnetic properties of Co–Fe–Ta–B bulk glassy alloys.* Acta Materialia, 2004. 52(6): p. 1631-1637.
3. Hostert, C., et al., *Ab initio molecular dynamics model for density, elastic properties and short range order of Co–Fe–Ta–B metallic glass thin films.* Journal of Physics: Condensed Matter, 2011. 23(47): p. 475401.
4. Lewandowski, J.J., et al., *Tough Fe-based bulk metallic glasses.* Appl. Phys. Lett., 2008. 92: p. 091918.
5. Rösner, H., et al., *Density changes in shear bands of a metallic glass determined by correlative analytical transmission electron microscopy.* Ultramicroscopy, 2014. 142 p. 1-9.
6. Schuh, C.A., T.C. Hufnagel, and U. Ramamurty, *Overview No.144 - Mechanical behavior of amorphous alloys.* Acta Materialia, 2007. 55(12): p. 4067-4109.
7. Greer, A.L., *4 - Metallic Glasses*, in *Physical Metallurgy (Fifth Edition)*, D.E.L. Hono, Editor. 2014, Elsevier: Oxford. p. 305-385.
8. Klement, W., R.H. Willens, and P.O.L. Duwez, *Non-crystalline Structure in Solidified Gold–Silicon Alloys.* Nature, 1960. 187(4740): p. 869-870.
9. Gilbert, C.J., J.M. Lippmann, and R.O. Ritchie, *Fatigue of a Zr-Ti-Cu-Ni-Be bulk amorphous metal: Stress/life and crack-growth behavior.* Scripta Materialia, 1998. 38(4): p. 537-542.
10. Heffelfinger, G.S., *Parallel atomistic simulations.* Computer Physics Communications, 2000. 128(1): p. 219-237.
11. Thomas, F., et al., *Atomistic simulations of complex materials: ground-state and excited-state properties.* Journal of Physics: Condensed Matter, 2002. 14(11): p. 3015.
12. Chen, L.-Q. and Y. Gu, *27 - Computational Metallurgy*, in *Physical Metallurgy (Fifth Edition)*, D.E.L. Hono, Editor. 2014, Elsevier: Oxford. p. 2807-2835.
13. Lewandowski, J.J., W.H. Wang, and A.L. Greer, *Intrinsic plasticity or brittleness of metallic glasses.* Philosophical Magazine Letters, 2005. 85(2): p. 77-87.
14. Schnabel, V., et al., *Electronic hybridisation implications for the damage-tolerance of thin film metallic glasses.* Scientific Reports, 2016. 6: p. 36556.
15. Inoue, A., *Bulk Glassy Alloys: Historical Development and Current Research.* Engineering, 2015. 1(2): p. 185-191.
16. Matsumoto, H., et al., *FePBNbCr soft-magnetic glassy alloys with low loss characteristics for inductor cores.* Journal of Alloys and Compounds, 2010. 504(0): p. S139-S141.
17. Zberg, B., P.J. Uggowitzer, and J.F. Loffler, *MgZnCa glasses without clinically observable hydrogen evolution for biodegradable implants.* Nat Mater, 2009. 8(11): p. 887-891.

References

18. Schroers, J., et al., *Bulk metallic glasses for biomedical applications.* JOM, 2009. 61(9): p. 21-29.
19. Tylecote, R.F., *A history of metallurgy* 1976, London , United Kingdom: The Metals Society
20. McLean, D., *A new field for materials science.* Materials Science and Engineering, 1976. 26(2): p. 141-152.
21. Laughlin, D.E. and K. Hono, *Preface to the Fifth Edition*, in *Physical Metallurgy (Fifth Edition)*, D.E.L. Hono, Editor. 2014, Elsevier: Oxford. p. ix-x.
22. Turnbull, D. and B. Vonnegut, *Nucleation Catalysis.* Industrial & Engineering Chemistry, 1952. 44(6): p. 1292-1298.
23. Greer, A.L., *Metallic glasses…on the threshold.* Materials Today, 2009. 12(1-2): p. 14-22.
24. Sheng, H.W., et al., *Atomic packing and short-to-medium-range order in metallic glasses.* Nature, 2006. 439(7075): p. 419-425.
25. Cahn, R.W. and A.L. Greer, *Chapter 19 - Metastable states of alloys*, in *Physical Metallurgy (Fourth, Revised and Enhanced Edition)*, R.W.C. Haasen†, Editor. 1996, North-Holland: Oxford. p. 1723-1830.
26. Axinte, E., *Metallic glasses from "alchemy" to pure science: Present and future of design, processing and applications of glassy metals.* Materials & Design, 2012. 35(0): p. 518-556.
27. Löffler, J.F., *Bulk metallic glasses.* Intermetallics, 2003. 11(6): p. 529-540.
28. Senkov, O.N., *Correlation between fragility and glass-forming ability of metallic alloys.* Physical Review B, 2007. 76(10).
29. Inoue, A., N. Nishiyama, and H. Kimura, *Preparation and Thermal Stability of Bulk Amorphous Pd40Cu30Ni10P20 Alloy Cylinder of 72 mm in Diameter.* Materials Transactions, JIM, 1997. 38(2): p. 179-183.
30. Inoue, A., *Bulk amorphous alloys with soft and hard magnetic properties.* Materials Science and Engineering a-Structural Materials Properties Microstructure and Processing, 1997. 226(0): p. 357-363.
31. Greer, A.L., *Metallic Glasses.* Science, 1995. 267(5206): p. 1947-1953.
32. Cahn, R.W., *Metallic Glasses - Some Current Issues.* Le Journal de Physique Colloques, 1982. 43(C9): p. C9-55-C9-66.
33. Mader, S., *Phase transformations in thin films.* Thin Solid Films, 1976. 35(2): p. 195-200.
34. Inoue, A., *Stabilization of metallic supercooled liquid and bulk amorphous alloys.* Acta Materialia, 2000. 48(1): p. 279-306.
35. Schaller, R.R., *Moore's law: past, present and future.* IEEE Spectrum, 1997. 34(6): p. 52-59.
36. Hostert, C., et al., *Quantum mechanically guided design of Co 43 Fe 20 Ta 5.5 X 31.5 (X=B, Si, P, S) metallic glasses.* Journal of Physics: Condensed Matter, 2012. 24(17): p. 175402.
37. Ozaki, T. and H. Kino, *Efficient projector expansion for theab initioLCAO method.* Physical Review B, 2005. 72(4).

38. Kresse, G. and J. Furthmüller, *Efficient iterative schemes forab initiototal-energy calculations using a plane-wave basis set.* Physical Review B, 1996. 54(16): p. 11169-11186.
39. Schnabel, V., et al., *Temperature-Induced Short-Range Order Changes in Co67B33Glassy Thin Films and Elastic Limit Implications.* Materials Research Letters, 2014. 3(2): p. 82-87.
40. Schnabel, V., et al., *Temperature-Induced Short-Range Order Changes in $Co_{67}B_{33}$ Glassy Thin Films and Elastic Limit Implications.* Mater. Res. Lett., 2015. 3(2): p. 82-87.
41. Argon, A.S., *Plastic deformation in metallic glasses.* Acta Metallurgica, 1979. 27(1): p. 47-58.
42. Conner, R.D., et al., *Shear bands and cracking of metallic glass plates in bending.* Journal of Applied Physics, 2003. 94(2): p. 904.
43. Turnbull, D. and M.H. Cohen, *Free-Volume Model of the Amorphous Phase: Glass Transition.* The Journal of Chemical Physics, 1961. 34(1): p. 120.
44. Schuh, C.A., T.C. Hufnagel, and U. Ramamurty, *Mechanical behavior of amorphous alloys.* Acta Mater., 2007. 55: p. 4067-4109.
45. Greer, A.L., Y.Q. Cheng, and E. Ma, *Shear bands in metallic glasses.* Mater. Sci. Eng., R, 2013. 74: p. 71-132.
46. Pan, D., et al., *Experimental characterization of shear transformation zones for plastic flow of bulk metallic glasses.* Proc Natl Acad Sci U S A, 2008. 105(39): p. 14769-72.
47. Zhang, Y. and A.L. Greer, *Thickness of shear bands in metallic glasses.* Applied Physics Letters, 2006. 89(7): p. 071907.
48. Shimizu, F., S. Ogata, and J. Li, *Yield point of metallic glass.* Acta Materialia, 2006. 54(16): p. 4293-4298.
49. Gao, Y.F., et al., *On the shear-band direction in metallic glasses.* Acta Materialia, 2011. 59(10): p. 4159-4167.
50. Xu, J., U. Ramamurty, and E. Ma, *The fracture toughness of bulk metallic glasses.* JOM, 2010. 62(4): p. 10-18.
51. Spaepen, F., *A microscopic mechanism for steady state inhomogeneous flow in metallic glasses.* Acta Metallurgica, 1977. 25(4): p. 407-415.
52. Greaves, G.N., et al., *Poisson's ratio and modern materials.* Nat Mater, 2011. 10(11): p. 823-37.
53. He, Q., et al., *Locating bulk metallic glasses with high fracture toughness: Chemical effects and composition optimization.* Acta Materialia, 2011. 59(1): p. 202-215.
54. Nollmann, N., et al., *Impact of micro-alloying on the plasticity of Pd-based bulk metallic glasses.* Scripta Materialia, 2016. 111: p. 119-122.
55. Kumar, G., et al., *Unusual brittle behavior of Pd-based bulk metallic glass.* Scripta Mater., 2011. 65: p. 585-587.
56. Raghavan, R., P. Murali, and U. Ramamurty, *On factors influencing the ductile-to-brittle transition in a bulk metallic glass.* Acta Mater., 2009. 57: p. 3332-3340.
57. Cheng, Y.Q. and E. Ma, *Atomic-level structure and structure–property relationship in metallic glasses.* Progress in Materials Science, 2011. 56(4): p. 379-473.

References

58. Biloni, H. and W.J. Boettinger, *Chapter 8- Solidification*, in *Physical Metallurgy (Fourth, Revised and Enhanced Edition)*, R.W.C. Haasen†, Editor. 1996, North-Holland: Oxford. p. 669-842.
59. Barbee, T.W., et al., *Synthesis of amorphous niobium-nickel alloys by vapor quenching.* Thin Solid Films, 1977. 45: p. 591-599.
60. Gebhardt, T., et al., *Influence of chemical composition and magnetic effects on the elastic properties of fcc Fe–Mn alloys.* Acta Materialia, 2011. 59(4): p. 1493-1501.
61. Schnabel, V., et al., *Revealing the relationships between chemistry, topology and stiffness of ultrastrong Co-based metallic glass thin films: A combinatorial approach.* Acta Materialia, 2016. 107: p. 213-219.
62. Oliver, W.C. and G.M. Pharr, *Measurement of hardness and elastic modulus by instrumented indentation: Advances in understanding and refinements to methodology.* Journal of Materials Research, 2011. 19(01): p. 3-20.
63. Fischer-Cripps, A.C., *Nanoindentation*. 2011. 1-19.
64. Matoy, K., et al., *A comparative micro-cantilever study of the mechanical behavior of silicon based passivation films.* Thin Solid Films, 2009. 518(1): p. 247-256.
65. Wurster, S., C. Motz, and R. Pippan, *Characterization of the fracture toughness of micro-sized tungsten single crystal notched specimens.* Philosophical Magazine, 2012. 92(14): p. 1803-1825.
66. Jaya, B.N., C. Kirchlechner, and G. Dehm, *Can microscale fracture tests provide reliable fracture toughness values? A case study in silicon.* Journal of Materials Research, 2015. 30(05): p. 686-698.
67. Biswas, K. and S. Kal, *Etch characteristics of KOH, TMAH and dual doped TMAH for bulk micromachining of silicon.* Microelectronics Journal, 2006. 37(6): p. 519-525.
68. Larson, D.J., et al., *Local Electrode Atom Probe Tomography*. 2013: Springer New York Heidelberg Dordrecht London. 328.
69. Kelly, T.F. and M.K. Miller, *Invited review article: Atom probe tomography.* Rev Sci Instrum, 2007. 78(3): p. 031101.
70. Müller, E.W., *The Atom-Probe Field Ion Microscope.* Review of Scientific Instruments, 1968. 39(1): p. 83.
71. Müller, E.W., *Abreissen adsorbierter Ionen durch hohe elektrische Feldstaerken.* Die Naturwissenschaften, 1941. 29(35): p. 533-534.
72. Gault, B., et al., *Atom Probe Microscopy*. Vol. 160. 2012: Springer New York Heidelberg Dordrecht London.
73. Bas, P., et al., *A general protocol for the reconstruction of 3D atom probe data.* Applied Surface Science, 1995. 87-88: p. 298-304.
74. Gault, B., et al., *Advances in the reconstruction of atom probe tomography data.* Ultramicroscopy, 2011. 111(6): p. 448-57.
75. Geiser, B.P., et al., *Wide-Field-of-View Atom Probe Reconstruction.* Microscopy and Microanalysis, 2009. 15(S2): p. 292-293.
76. Miller, M.K. and R.G. Forbes, *Atom-Probe Tomography: The Local Electrode Atom Probe*. 2014: Springer New York Heidelberg Dordrecht London.
77. Müller, E.W., *Field Desorption.* Physical Review, 1956. 102(3): p. 618-624.

78. Haley, D., et al., *Influence of field evaporation on Radial Distribution Functions in Atom Probe Tomography.* Philosophical Magazine, 2009. 89(11): p. 925-943.
79. Sha, G. and A. Cerezo, *Field ion microscopy and 3-D atom probe analysis of Al3Zr particles in 7050 Al alloy.* Ultramicroscopy, 2005. 102(2): p. 151-9.
80. Miller, M.K., L. Longstreth-Spoor, and K.F. Kelton, *Detecting density variations and nanovoids.* Ultramicroscopy, 2011. 111(6): p. 469-72.
81. Rose, D.J., *On the Magnification and Resolution of the Field Emission Electron Microscope.* Journal of Applied Physics, 1956. 27(3): p. 215.
82. De Geuser, F., et al., *Correlated field evaporation as seen by atom probe tomography.* Surface Science, 2007. 601(2): p. 536-543.
83. Elswijk, H.B., P.M. Bronsveld, and J.T.M. De Hosson, *Field Ion Microscope, Imaging Atom Probe Study of Metallic Glasses.* Le Journal de Physique Colloques, 1987. 48(C6): p. C6-305-C6-310.
84. Godfrey, T.J., et al., *The Characterization of Spinodal Structures in Duplex Cf3 Steels.* Le Journal de Physique Colloques, 1988. 49(C6): p. C6-421-C6-426.
85. Moody, M.P., et al., *Quantitative binomial distribution analyses of nanoscale like-solute atom clustering and segregation in atom probe tomography data.* Microsc Res Tech, 2008. 71(7): p. 542-50.
86. Thompson, K., et al., *In situ site-specific specimen preparation for atom probe tomography.* Ultramicroscopy, 2007. 107(2-3): p. 131-9.
87. Hono, K. and S.S. Babu, *15 - Atom-Probe Field Ion Microscopy*, in *Physical Metallurgy (Fifth Edition)*, D.E.L. Hono, Editor. 2014, Elsevier: Oxford. p. 1453-1589.
88. Williams, D.B. and C.B. Carter, *Transmission Electron Microscopy*. 2009: Springer.
89. Brandon, D. and W.D. Kaplan, *Microstructural characterization of materials*. 2013: John Wiley & Sons.
90. Fraser, H.L., D.W. McComb, and R.E.A. Williams, *12 - Transmission Electron Microscopy for Physical Metallurgists*, in *Physical Metallurgy (Fifth Edition)*, D.E.L. Hono, Editor. 2014, Elsevier: Oxford. p. 1143-1226.
91. Carter, C.B. and D.B. Williams, *Transmission Electron Microscopy*. 2016, Switzerland: Springer International Publishing.
92. Schmidt, V., et al., *Quantitative Measurement of Density in a Shear Band of Metallic Glass Monitored Along its Propagation Direction.* Phys Rev Lett, 2015. 115(3): p. 035501.
93. Giannuzzi, L.A. and F.A. Stevie, *A review of focused ion beam milling techniques for TEM specimen preparation.* Micron, 1999. 30(3): p. 197-204.
94. Schaffer, M., B. Schaffer, and Q. Ramasse, *Sample preparation for atomic-resolution STEM at low voltages by FIB.* Ultramicroscopy, 2012. 114: p. 62-71.
95. Herbig, M., P. Choi, and D. Raabe, *Combining structural and chemical information at the nanometer scale by correlative transmission electron microscopy and atom probe tomography.* Ultramicroscopy, 2015. 153: p. 32-39.
96. Gu, X.J., et al., *Mechanical properties, glass transition temperature, and bond enthalpy trends of high metalloid Fe-based bulk metallic glasses.* Applied Physics Letters, 2008. 92(16): p. 161910.

References

97. Schnabel, V., et al., *Stiffness and toughness prediction of Co-Fe-Ta-B metallic glasses, alloyed with Y, Zr, Nb, Mo, Hf, W, C, N and O by ab initio molecular dynamics.* J. Phys.: Condens. Matter, 2015. 27: p. 105502.
98. Kostorz, G., *Chapter 12 - X-ray and neutron scattering*, in *Physical Metallurgy (Fourth, Revised and Enhanced Edition)*, R.W.C. Haasen†, Editor. 1996, North-Holland: Oxford. p. 1115-1199.
99. Thomas, J. and T. Gemming, *Analytische Transmissionselektronenmikroskopie*. 2013: Springer-Verlag Wien 2013.
100. Dr. G. W. H. Höhne, W.F.H., H.-J. Flammersheim, *Differential Scanning Calorimetry*. 2nd edition, ed. C. Messerschmidt. 2003: Springer Berlin Heidelberg.
101. Jaya, B.N. and V. Jayaram, *Crack stability in edge-notched clamped beam specimens: modeling and experiments.* International Journal of Fracture, 2014. 188(2): p. 213-228.
102. Holm, B., et al., *Elastic and optical properties ofα- andκ–Al2O3.* Physical Review B, 1999. 59(20): p. 12777-12787.
103. Schnabel, V., *Stiff and damage-tolerant metallic glasses*, in *Fakultät für Georessourcen und Materialtechnik*. 2016, Rheinisch-Westfälischen Technischen Hochschule Aachen: Thesis.
104. Madge, S.V., et al., *Toughness, extrinsic effects and Poisson's ratio of bulk metallic glasses.* Acta Mater., 2012. 60: p. 4800-4809.
105. Xi, X.K., et al., *Fracture of Brittle Metallic Glasses: Brittleness or Plasticity.* Phys. Rev. Lett., 2005. 94: p. 125510.
106. He, Q., et al., *Locating bulk metallic glasses with high fracture toughness: Chemical effects and composition optimization.* Acta Mater., 2011. 59: p. 202-215.
107. Lewandowski, J.J., W.H. Wang, and A.L. Greer, *Intrinsic plasticity of brittleness of metallic glasses.* Philos. Mag. Lett., 2005. 85: p. 77-87.
108. Mecholsky, J.J., R.W. Rice, and S.W. Freiman, *Prediction of Fracture Energy and Flaw Size in Glasses from Measurements of Mirror Size.* J. Am. Ceram. Soc., 1974. 57: p. 440-443.
109. Jia, P., et al., *Notch toughness of Cu-based bulk metallic glasses.* Scripta Mater., 2009. 61: p. 137-140.
110. Wesseling, P., et al., *Preliminary assessment of flow, notch toughness, and high temperature behavior of* $Cu_{60}Zr_{20}Hf_{10}Ti_{10}$ *bulk metallic glass.* Scripta Mater., 2004. 51: p. 151-154.
111. Schroers, J. and W.L. Johnson, *Ductile Bulk Metallic Glass.* Phys. Rev. Lett., 2004. 93: p. 255506.
112. Guin, J.-P., T. Rouxel, and J.-C. Sangleboeuf, *Hardness, Toughness, and Scratchability of Germanium–Selenium Chalcogenide Glasses.* J. Am. Ceram. Soc., 2002. 85(6): p. 1545-1552.
113. Ashby, M. and A. Greer, *Metallic glasses as structural materials.* Scripta Materialia, 2006. 54(3): p. 321-326.
114. Ashby, M., *Materials Selection in Mechanical Design*. Third Edition ed. 2005, Oxford: Elsevier.

115. Chen, C.Q., Y.T. Pei, and J.T.M. De Hosson, *Effects of size on the mechanical response of metallic glasses investigated through in situ TEM bending and compression experiments.* Acta Materialia, 2010. 58(1): p. 189-200.
116. Bharathula, A., et al., *Compression testing of metallic glass at small length scales: Effects on deformation mode and stability.* Acta Materialia, 2010. 58(17): p. 5789-5796.
117. Jang, D.C., C.T. Gross, and J.R. Greer, *Effects of size on the strength and deformation mechanism in Zr-based metallic glasses.* International Journal of Plasticity, 2011. 27(6): p. 858-867.
118. Dunham, A.C. and F.C.F. Wilkinson, *Accuracy, precision and detection limits of energy-dispersive electron-microprobe analyses of silicates.* X-Ray Spectrometry, 1978. 7(2): p. 50-56.
119. V. Schnabel, M.K., D. Music, J. Bednarcik, W. J. Clegg, D. Raabe, J. M. Schneider, *Stiffness of bulk and thin film metallic glasses defined by bond strength density*, in *preparation*. 2016.
120. Guo, W., et al., *Deformation induced alloying in crystalline – metallic glass nano-composites.* Materials Science and Engineering: A, 2015. 628: p. 269-280.
121. Zhang, Y., et al., *Composition effect on intrinsic plasticity or brittleness in metallic glasses.* Sci Rep, 2014. 4: p. 5733.
122. Shibata, A., M. Sone, and Y. Higo, *Characterization of deformation-induced structural change of Pd78Cu6Si16 metallic glass using a micro-sized cantilever-beam specimen.* Scripta Materialia, 2010. 62(5): p. 309-312.
123. Polk, D.E. and D. Turnbull, *Flow of melt and glass forms of metallic alloys.* Acta Metallurgica, 1972. 20(4): p. 493-498.
124. Yavari, A.R., et al., *Excess free volume in metallic glasses measured by X-ray diffraction.* Acta Materialia, 2005. 53(6): p. 1611-1619.
125. Dmowski, W., et al., *Structural rejuvenation in a bulk metallic glass induced by severe plastic deformation.* Acta Materialia, 2010. 58(2): p. 429-438.
126. Klaumünzer, D., et al., *Probing shear-band initiation in metallic glasses.* Phys Rev Lett, 2011. 107(18): p. 185502.
127. Sahu, K.K., et al., *Phase separation mediated devitrification of Al88Y7Fe5 glasses.* Acta Materialia, 2010. 58(12): p. 4199-4206.
128. Nowak, C., G. Schmitz, and R. Kirchheim, *Electric field effect on low temperature nanoscale oxidation.* Surface Science, 2010. 604(7-8): p. 641-648.
129. Spaepen, F., *Metallic glasses: Must shear bands be hot?* Nat Mater, 2006. 5(1): p. 7-8.
130. Yang, B., et al., *In-situ thermographic observation of mechanical damage in bulk-metallic glasses during fatigue and tensile experiments.* Intermetallics, 2004. 12(10–11): p. 1265-1274.
131. Yang, B., et al., *Dynamic evolution of nanoscale shear bands in a bulk-metallic glass.* Applied Physics Letters, 2005. 86(14): p. 141904.
132. Klaumünzer, D., R. Maaß, and J.F. Löffler, *Stick-slip dynamics and recent insights into shear banding in metallic glasses.* Journal of Materials Research, 2011. 26(12): p. 1453-1463.

References

133. Song, S.X., X.L. Wang, and T.G. Nieh, *Capturing shear band propagation in a Zr-based metallic glass using a high-speed camera.* Scripta Materialia, 2010. 62(11): p. 847-850.
134. Bengus, V.Z., et al., *Some peculiarities of ductile shear failure of amorphous alloy ribbons.* International journal of rapid solidification, 1993. 8(1): p. 21-31.
135. Chen, H., et al., *Deformation-induced nanocrystal formation in shear bands of amorphous alloys.* Nature, 1994. 367(6463): p. 541-543.
136. Zhang, T. and H. Men, *Plastic deformability and precipitation of nanocrystallites during compression for a Cu–Zr–Ti–Sn bulk metallic glass.* Journal of Alloys and Compounds, 2007. 434–435: p. 10-12.
137. Boucharat, N., et al., *Synthesis routes for controlling the microstructure in nanostructured Al88Y7Fe5 alloys.* Journal of Alloys and Compounds, 2007. 434–435: p. 252-254.
138. Greer, A.L., K.L. Rutherford, and I.M. Hutchings, *Wear resistance of amorphous alloys and related materials.* International Materials Reviews, 2002. 47(2): p. 87-112.
139. Lewandowski, J.J., et al., *Tough Fe-based bulk metallic glasses.* Applied Physics Letters, 2008. 92(9): p. 091918.
140. Laboratory_of_glass_Science. *SPP 1594 - Topological Engineering of Ultrastrong Glasses*. 2016; Available from: http://www.spp1594.uni-jena.de/Imprint.html.
141. Pang, S.J., et al., *Synthesis of Fe–Cr–Mo–C–B–P bulk metallic glasses with high corrosion resistance.* Acta Materialia, 2002. 50(3): p. 489-497.
142. Pardo, A., et al., *The influence of Cr addition on the corrosion resistance of Fe73.5Si13.5B9Nb3Cu1 metallic glass in marine environments.* Corrosion Science, 2002. 44(6): p. 1193-1211.
143. Peter, W.H., et al., *Localized corrosion behavior of a zirconium-based bulk metallic glass relative to its crystalline state.* Intermetallics, 2002. 10(11–12): p. 1157-1162.
144. Sridhara_Rao, D.V., K. Muraleedharan, and C.J. Humphreys, *TEM specimen preparation techniques.* Microscopy: Science, Technology, Applications and Education, 2010.
145. Inoue, A., T. Zhang, and T. Masumoto, *Production of Amorphous Cylinder and Sheet of La55A25Ni20 Alloy by a Metallic Mold Casting Method.* Materials Transactions, JIM, 1990. 31(5): p. 425-428.
146. Gottstein, G., *Physikalische Grundlagen der Materialkunde*. 2007, Heidelberg: Springer Berlin Heidelberg.